

1 **Emplacement of shergottites in the martian crust inferred from 3D petrofabric and crystal**
2 **size distribution analyses**

3
4 S. A. Eckley^{1,2*}, R. A. Ketcham², Y. Liu³, J. Gross^{4,5,6,7}, F. M. McCubbin⁷

5
6 ¹Jacobs – JETS, Astromaterials Research and Exploration Science Division, NASA Johnson
7 Space Center, Houston, TX, USA

8 ²Jackson School of Geosciences, The University of Texas at Austin, Austin, TX, USA

9 ³Jet Propulsion Laboratory, California Institute of Technology, Pasadena, CA, USA

10 ⁴Department of Earth and Planetary Sciences, Rutgers University, Piscataway, NJ, USA

11 ⁵Department of Earth and Planetary Sciences, American Museum of Natural History, New York,
12 NY, USA

13 ⁶Lunar and Planetary Institute, Houston, TX, USA

14 ⁷NASA Johnson Space Center, Houston, TX, USA

15
16 *Corresponding author's email: scott.a.eckley@nasa.gov and phone #: +1 281 483 1157

17
18 **Abstract** - Shergottites are mafic to ultramafic igneous rocks that represent a majority of known
19 martian meteorites. They are subdivided into gabbroic, poikilitic, basaltic, and olivine-phyric
20 categories based on differences in mineralogy and textures. Their geologic contexts are unknown
21 so analyses of crystal sizes and preferred orientations have commonly been used to infer where
22 shergottites solidified. Such environments range from subsurface cumulates to shallow intrusives
23 to extrusive lava flows, which all have contrasting implications for interactions with crustal
24 material, cooling histories, and potential in situ exposure at the surface. In this study, we present
25 a novel three-dimensional (3D) approach to better understand the solidification environments of
26 these samples and improve our knowledge of shergottites' geologic contexts. Shape preferred
27 orientations of most phases and crystal size distributions of late-forming minerals were measured
28 in 3D using X-ray computed tomography (CT) on eight shergottites representing the gabbroic,
29 poikilitic, basaltic, and olivine-phyric categories. Our analyses show that highly anisotropic, rod-
30 like pyroxene crystals are strongly foliated in the gabbroic samples but have a weaker foliation
31 and a mild lineation in the basaltic sample, indicating a directional flow component in the latter.
32 Star volume distribution analyses revealed that most phases (maskelynite, pyroxene, olivine, and
33 oxides/sulfides) preserve a foliated texture with variable strengths, and that the phases within
34 individual samples are strongly to moderately aligned with respect to one another. In
35 combination with relative cooling rates during the final stages of crystallization determined from
36 interstitial oxide/sulfide crystal size distribution analyses, these results indicate that the olivine-
37 phyric samples were emplaced as shallow intrusives (e.g., dikes/sills) and that the gabbroic,
38 poikilitic, and basaltic samples were emplaced in deeper subsurface environments.

39
40 **INTRODUCTION**

41 Martian meteorites are currently the only physical materials from Mars that can be
42 studied in the laboratory and have provided a wealth of information on the planet's geologic
43 history. They are nearly all igneous rocks with mafic to ultramafic compositions and have been
44 divided into three main categories — shergottites, nakhlites, and chassignites — with
45 shergottites comprising a vast majority with nearly 300 individual named stones to date
46 (Gattacceca et al. 2023, McSween 2015, Udry et al. 2020). Shergottites are subdivided into four

47 groups based on textural and mineralogical characteristics: basaltic, gabbroic, olivine-phyric, and
48 poikilitic (e.g., Udry et al. 2020). In addition to textural differences, the shergottites are
49 subdivided into three geochemical groups based on their bulk trace element and isotope
50 geochemistry: geochemically enriched, intermediate, and depleted (Barnes et al. 2020,
51 Sarbadhikari et al. 2011, Shearer et al. 2013, Tait and Day 2018). Regardless of lithology or
52 geochemistry, most, if not all, shergottites experienced complex crystallization histories
53 characterized by episodes of cooling and crystal growth at various depths throughout the martian
54 crust with a final period of cooling and solidification during emplacement in the shallow
55 subsurface or eruption onto the surface (Balta et al. 2015, Filiberto et al. 2018, First and Hammer
56 2016, Gross et al. 2013b, Gross et al. 2011, Howarth et al. 2014, Lentz and McSween 2000, Liu
57 et al. 2013, Liu et al. 2016, McCoy et al. 1992, Rahib et al. 2019, Udry et al. 2017, Usui et al.
58 2008, Usui et al. 2010). Shergottites represent the largest and most diverse sampling of martian
59 secondary crustal material on Earth and provide a window into volcanic processes on Mars.

60 Terrestrial volcanic systems can have a complex topology featuring multiple magma
61 chambers, conduits, dikes, cone sheets, and/or sills emplaced in the subsurface (Tibaldi 2015). If
62 the magma erupts onto the surface, lava flows, tubes, and ponds of various morphologies can
63 form (Crisp 1984). Both subsurface and surface volcanic features can have a wide range of
64 thicknesses and lateral extents and subsurface features can be emplaced at a variety of depths.
65 Because magma can solidify in any of these environments, igneous rocks with the same bulk
66 composition can display considerable textural diversity. This holds true for shergottites, but their
67 various geological contexts are obscured by the fact that they were ejected from the martian
68 near-surface during impact events. Textural and geochemical analyses of shergottites can provide
69 an opportunity to investigate the final stages of their parent melts' crystallization histories, which
70 are then used to infer modes of magma emplacement or eruption and the structure of volcanic
71 systems on Mars.

72 Basaltic and gabbroic shergottites are mineralogically similar, with pyroxene and
73 plagioclase (now maskelynite) as the dominant phases. The coarser texture of the gabbroic
74 shergottites (average pyroxene length of 1 mm, up to 5 mm) (e.g., Udry et al. 2020) is interpreted
75 to reflect prolonged and slower crystallization and solidification at greater depths (Filiberto et al.
76 2018, Wenzel et al. 2021) compared to the finer-grained basaltic shergottites (average pyroxene
77 length of 0.3 mm, up to 1 mm) (e.g., Udry et al. 2020), which are variably interpreted to have
78 solidified in environments ranging from hypabyssal (shallow intrusives) to thin or thick extrusive
79 flows (Lentz and McSween 2000, McCoy et al. 1992, Mcsween et al. 1996, Smith and Hervig
80 1979, Stolper and McSween 1979). Olivine-phyric shergottites have porphyritic textures with
81 early-formed megacryst (0.5 – 3.0 mm) olivine that crystallized in the lower crust. These are set
82 in fine-grained to glassy groundmasses that are interpreted to have solidified in a large range of
83 hypabyssal to extrusive environments (Ennis and McSween 2014, First and Hammer 2016, Gross
84 et al. 2011, Liu et al. 2013, Liu et al. 2016, Sarbadhikari et al. 2009, Usui et al. 2008). Poikilitic
85 shergottites are characterized by having olivine chadacrysts enclosed by large (cm-sized)
86 pyroxene oikocrysts, set in a coarse-grained groundmass consisting of olivine, pyroxene, and
87 plagioclase (now maskelynite). The poikilitic olivine-pyroxene assemblages are interpreted to
88 have formed in the lower crust and the groundmass crystallized during ascent and final
89 emplacement as a coarse-grained intrusive rock (Combs et al. 2019, Howarth et al. 2014,
90 McSween and Treiman 1998, Rahib et al. 2019).

91 Most interpretations of how shergottite parent melts were emplaced or erupted cited
92 above are based on analyses of crystal sizes and measurements of mineral shape preferred

93 orientations (SPO). There is a significant variation in crystal sizes, even within the same
94 shergottite subgroups, indicating that a single solidification environment may not be applicable
95 for all samples belonging to a specific lithologic category. Further complications arise from the
96 fact that crystal size distribution (CSD) analyses have, thus far, been only extrapolated from two-
97 dimensional (2D) data, which assumes a mineral's common habits and hence can hinder accurate
98 interpretations when the mineral grows out of equilibrium. Similarly, all SPO measurements
99 have been made on traditional thin/thick sections, limiting their analyses to 2D (Duke 1968,
100 Filiberto et al. 2018, Greshake et al. 2004, Smith and Hervig 1979, Stolper and McSween 1979).
101 Without three orthogonal sections, which is uncommon for these rare and typically small
102 samples, interpretations of 2D SPO analyses are limited. Three-dimensional crystallographic
103 preferred orientations (CPO) have been made on shergottites (Orr et al. 2022) and nakhlites
104 (Griffin et al. 2022), a suite of martian clinopyroxene cumulate meteorites unrelated to the
105 shergottites, using electron backscatter diffraction (EBSD) analysis.

106 In this study, we examine 3D textures in eight shergottites using X-ray computed
107 tomography (CT) (Fig. 1). The samples were selected to represent all lithologic groupings and
108 provide the largest range of igneous textures. We investigate fabrics of several phases and crystal
109 size distributions of combined oxides and sulfides to derive stress/deformation conditions and
110 relative cooling rates during the final stages of crystallization, respectively. We use this
111 information to infer where in the martian crust these samples solidified, which is important for
112 characterizing the structure of volcanic systems on Mars, determining possible interactions
113 between shergottites and other crustal rocks or subsurface fluids at magmatic and subsolidus
114 temperatures, and identifying rock types that may be present at or near the surface.

115 116 **SAMPLES AND ANALYTICAL METHODS**

117 **Samples**

118 *Olivine-phyric*

119 Small (<5 g) chips embedded in a 1-inch epoxy disc were obtained from the Meteorite
120 Working Group for samples Larkman Nunatak (LAR) 12095(40A), LAR 12011(54A), and
121 Elephant Moraine (EETA) 79001(536) lithology A. Their exact masses are unknown because
122 thin and thick sections of unknown masses were previously prepared from these embedded
123 samples. A 2.24 g chip of Tissint was given to M. Fries from the Dupont meteorite collection at
124 the Chicago Field Museum, who in turn made it available for this study. Of these samples, LAR
125 12095, EETA 79001 lithology A, and Tissint are all geochemically depleted shergottites, and
126 LAR 12011 is a geochemically enriched shergottite (Tait and Day 2018). A summary of
127 previously published descriptions for all analyzed samples is found in Supplementary Material
128 (Section A) (DOI: 10.17632/mzgp37947y.1).

129 130 *Basaltic*

131 An ~4 g chip of Zagami was obtained from the University of New Mexico Institute of
132 Meteoritics. Zagami is an enriched shergottite (Borg and Draper 2003).

133 134 *Gabbroic*

135 An ~9 g chip of Northwest Africa (NWA) 6963 was purchased by J. Gross from a dealer
136 in Morocco in 2016, and a 13.5 g piece of NWA 13134 was purchased by Y. Liu from a dealer in
137 2013 after being found in Morocco in 2012. Both NWA 6963 and NWA 13134 are enriched
138 shergottites (Burney et al. 2022, Filiberto et al. 2018).

139 *Poikilitic*

140 The entire mass (35.72 g) of Roberts Massif (RBT) 04261 was scanned as part of the
141 Astromaterials 3D project (Blumenfeld et al. 2019), and those data were used in this study. RBT
142 04261 is an enriched shergottite (Usui et al. 2010).

143

144 **X-ray Computed Tomography**

145 X-ray CT scanning was performed at the Astromaterials X-ray Fluorescence and
146 Computed Tomography (X-FaCT) Lab at NASA Johnson Space Center, the University of Texas
147 High-Resolution X-ray Computed Tomography Facility (UTCT), and the Analysis and Test Lab
148 at NASA Jet Propulsion Laboratory. Scanning conditions and instrumentation are summarized in
149 Table 1 and Supplementary Material (Section B). Software corrections were used to reduce beam
150 hardening and ring artifacts during reconstruction. The final reconstructed data are output as a
151 contiguous series of 2D (X and Y) 16-bit grayscale images (slices) oriented orthogonally to the
152 scan rotation axis (Z), which together comprise a 3D grid of cubic voxels (pixels with a third
153 dimension). Each voxel value (CT number) reflects the effective X-ray attenuation of the
154 material comprising that voxel, which is a function of the mean atomic number (z) and mean
155 density of the material, as well as the X-ray energy. Air is the least X-ray attenuating phase and
156 sets the baseline CT #. Phases with a higher relative X-ray attenuation (i.e. high- z and high
157 density) are assigned a higher CT #, and are generally visualized with brighter gray values
158 (Ketcham and Carlson 2001).

159

160 **X-ray CT data analysis**

161 *Interpreting CT #'s*

162 There is no direct correlation of CT #'s to specific phases because the X-ray beam is
163 polychromatic and beam energy varies with location within a sample due to beam hardening. As
164 a result, prior knowledge or complementary petrographic analysis of the sample is required to
165 map mineralogy. As shergottites have a primarily mafic/ultramafic mineralogy and have been
166 extensively studied (see Supplementary Material (Section A)), the dominant phases are known to
167 be plagioclase (now maskelynite) + pyroxene (mostly augite and pigeonite) + oxides/sulfides
168 (mostly titanomagnetite and ilmenite and pyrrhotite, respectively) \pm olivine (forsterite content
169 usually ranges from \sim Fo₅₀ to Fo₇₅). Phosphates (apatite and merrillite) and impact-melt glass
170 commonly comprise <3 vol.% (Shearer et al. 2015). Figure S1 shows the linear X-ray
171 attenuation coefficient (μ) for common shergottite phases at 80 keV obtained using MuCalc
172 (Hanna and Ketcham 2017), which calculates X-ray attenuation at different X-ray energies using
173 the NIST XCOM database.

174 All samples feature small, high-attenuation phases, such as oxides and sulfides and some
175 geochemically enriched samples have other trace minerals with high- μ components such as
176 baddeleyite (Moser et al. 2013, Staddon et al. 2021). Distinguishing between these phases in the
177 CT data is problematic because their CT #'s largely overlap (Fig. S1) and, due to their small
178 sizes relative to the size of the whole rock, their grayscales will be affected by blurring and
179 partial-volume effects with surrounding material. Accordingly, we group them together as “high-
180 μ phases.”

181

182 *Machine learning segmentation*

183 Digitally segmenting each CT dataset, which requires assigning each voxel to a specific
184 phase category, is required for object-based quantitative analysis. This is commonly done using a

185 global CT # threshold where a range of CT #'s corresponds to a single phase. However, this is
186 not possible for these samples because there is overlap in the CT #'s for pyroxenes, olivine,
187 phosphates, and basaltic glass (Fig. S1). To overcome CT # overlap, as well as other issues such
188 as mineral zoning and partial-volume effects inherent to CT scanning, we used machine learning
189 to segment the CT datasets. See Supplementary Material (Section C) for further details about
190 interpreting CT #'s and data segmentation. We used Dragonfly™ software's (Object Research
191 Systems) "Segmentation Trainer" tool to train a classifier on a limited number of manually
192 segmented slices (usually 5 to 30 slices) to enable automatic segmentation of the entire dataset.
193 During training, all voxels were manually assigned to one of five phase categories based on CT
194 #'s and observed petrologic textures: air (both internal voids and external air), maskelynite,
195 pyroxene, olivine, and high- μ phases. Even though pyroxene and olivine have overlapping CT
196 #'s, olivine are easy to distinguish because of their large size, morphology, and/or distinct zoning
197 patterns. Additionally, we could not identify phosphates or impact melt pockets or veins because
198 their ranges of CT #'s overlap with the primary phases and the phosphate grain sizes are near or
199 below the resolution limits. The training slices were used as inputs to the Extra-Trees classifying
200 engine, utilizing the smoothing, neighbors, morphological, median, and moments mathematical
201 filters. Once the classifier was sufficiently trained (i.e., automatically segmented >98% of the
202 manually segmented voxels correctly), it was used to automatically segment the entire CT
203 dataset. A new classifier was trained for each sample. However, even after extensive iterative
204 training, some of the Mg-rich olivine cores in the olivine-phyric samples were improperly
205 segmented as pyroxene because of their overlapping CT #'s and similar textures. As a final
206 processing step after machine learning classification, olivines with incorrectly segmented cores
207 were manually filled to add the mislabeled voxels to the olivine category. The final segmented
208 dataset is a binarized 3D phase map of air, maskelynite, pyroxene, olivine (if present), and high-
209 μ phases.

210

211 *Measuring modal abundances*

212 Normalized modal abundances were measured using the segmented data in *ImageJ*
213 software. Whole-rock modal abundances were determined by counting the number of voxels
214 assigned to each phase and normalizing to the total number of non-air voxels in the entire CT
215 dataset. To enable comparison with other studies that have utilized traditional modal analysis
216 based on 2D thin sections, we also calculated the modal abundance on a slice-by-slice basis
217 along the three orthogonal scan axes (XY, XZ, and YZ) (see Supplementary Material (Section
218 D)). Samples were not specially oriented during CT scanning, so the orthogonal axes are
219 random.

220

221 *CT fabric measurements*

222 Petrofabrics can be measured for each phase in a sample, and different quantification
223 methods are available based on whether the particular phase being examined is treated as a
224 continuum feature, or can be separated into individual mineral grains. We refer to the former as
225 continuum fabrics, and the latter as discrete fabrics, and both as CT fabrics in this paper. Both
226 approaches can provide the type, strength, and direction of preferred orientations, with the
227 principal difference that the discrete fabrics will honor grain boundaries and the continuum
228 fabrics will not. However, as phases constituting high modal percentages can be laborious,
229 problematic, or impossible to separate reliably into grains in CT data, the continuum approach
230 can provide information on more phases, more repeatably and with less effort. As such, we

231 measured continuum fabrics for maskelynite, pyroxene, olivine (if present), and high- μ phases in
232 all samples and discrete fabrics for high- μ phases (all samples) and pyroxenes (basaltic and
233 gabbroic samples). To facilitate comparing different measurements, all fabrics were
234 parameterized using K and C (Woodcock and Naylor 1983), which quantify the fabric type and
235 strength, respectively. Fabric strength (C) increase with the degree of anisotropy from zero
236 (isotropic) to infinity, and the shape parameter (K) ranges from zero to infinity and defines fabric
237 shapes (lineation [$K > 1$], foliation [$K < 1$], triaxial [$K = 1$]). A description of the fabric
238 parameters and how to calculate them for each CT fabric quantification method are given in
239 Supplementary Material (Section F and G).

240

241 *Continuum fabrics*

242 Continuum fabrics were measured on the segmented 3D datasets using Quant3D software
243 (Ketcham and Ryan 2004, Ketcham 2005b). Olivine crystals in the olivine-phyric shergottites
244 that are cross-cut by the sample boundary were manually removed from the segmented dataset to
245 prevent measurement of these incomplete crystals. This software integrates data from thousands
246 of discrete measurements to quantify the fabric of the segmented phase. Analytical details and a
247 description of the method are provided in Supplementary Material (Section E). The output data
248 are summarized by a second-rank tensor which provides three orthogonal principal component
249 directions (eigenvectors) and magnitudes (eigenvalues) and a 3D rose diagram is created to aid in
250 detection of non-orthogonal sub-fabric components. Because test point placement is random in
251 Quant3D, the analysis was repeated thirty times for each phase to assess statistical variation.
252 Figure 2 shows a simplified 2D schematic illustrating the Quant3D workflow.

253 The first, second, and third eigenvectors from the thirty replicate analyses for each phase
254 were plotted using Stereonet11 software (Cardozo and Allmendinger 2013). Replicate analyses
255 were plotted to map out confidence regions for each eigenvector and to aid in interpretation of
256 fabric types. Clustered first eigenvectors with girdled second and third eigenvectors indicates a
257 lineation, whereas clustered third eigenvectors and girdled first and second eigenvectors
258 indicates a foliation. Triaxial fabrics are characterized by clustering of all eigenvectors. The
259 average orientation of the 30 replicate analyses was calculated for each eigenvector to compare
260 the CT fabric orientation of one phase to another within the same sample. A description of
261 calculating the angle between CT fabrics within a sample is provided in Supplementary Material
262 (Section H).

263

264 *Discrete fabrics*

265 Pyroxenes in basaltic and gabbroic shergottites feature a texture of intermixed, elongated
266 crystals broken along multiple fractures (Fig. 1e-g). These could only be measured manually in
267 the 3D data, so we created a method for extracting a representative, non-biased sample. Using
268 Dragonfly, a crystal was randomly chosen and the CT data were reoriented along three
269 orthogonal views to expose its longest, intermediate, and shortest axes (Fig. 3b-d). We were only
270 interested in measuring long axis length and orientation, so instead of manually segmenting all
271 voxels comprising a single crystal, a rod was drawn through the crystal center along its length
272 using the 3D spherical brush tool (Fig. 3a). The diameter of the rod was smaller than the
273 diameter of the actual crystal to minimize touching of interlocking crystals. To prevent bias
274 based on crystal size or orientation, the 'cine' tool was used to randomly orient the data after
275 each crystal segmentation. The segmented data were imported into Blob3D software (Ketcham
276 2005a) where the few touching rods were manually separated, after which the length (BoxA

277 dimension) and orientation of each crystal long axis was measured. Long axis orientations of
278 every measured crystal were plotted using Stereonet11 software, and their spatial distributions
279 quantified by three eigenvalues and eigenvectors using the Bingham axial distribution analysis
280 (Fisher et al. 1993). These eigenvalues parameterize discrete CT fabrics with the K and C values
281 described above (see Supplementary Material (Section G) for calculating discrete CT fabric
282 parameters). This method, whereby a single 3D shape is used to approximate a phase's length
283 and orientation, is most effective with objects that have highly regular and anisotropic
284 morphologies (e.g., rods or plates). Measuring a phase's true shape, as in Fig. 3a, requires
285 segmenting all of its constituent voxels. This approach, or drawing at least three orthogonal
286 planes and fitting an ellipsoid (e.g., Hanna et al. 2015), is often required for phases with more
287 equant or irregular morphologies.

288

289 *Measuring highly attenuating phases*

290 We also measured the size and orientation of every individual high- μ phase using Blob3D
291 software (Ketcham 2005a) to: (1) calculate their 3D crystal size distribution (CSD) and (2)
292 provide an additional fabric measurement to corroborate the other continuum and discrete CT
293 fabrics. Only interstitial high- μ phases within the groundmass were measured; high- μ phases
294 included within larger minerals (i.e., pyroxene oikocrysts and olivine megacrysts) were excluded
295 from measurement, as we are only interested in grains whose orientations could be influenced by
296 flow and may reflect late-stage growth during the final period of crystallization. We used the
297 unsegmented grayscale data for these analyses because these phases within CT data are small
298 with respect to the sample size, and thus affected by partial-volume and blurring effects (PVB)
299 (Ketcham and Mote 2019), which Blob3D corrects for by using grayscale rather than segmented
300 data, resulting in more accurate ellipsoid and caliper dimensions. A description of isolating only
301 interstitial phases for measurement as well as the Blob3D methods is found in Supplementary
302 Material (Section I).

303 Similar to the discrete pyroxene fabrics described above, the long, intermediate, and short
304 axis orientation of each high- μ crystal was plotted using Stereonet11 and the distribution of each
305 axis quantified by a single set of eigenvalues and eigenvectors. Eigenvalues were used to
306 parameterize discrete CT fabrics with K and C. The primary eigenvector was used to represent
307 the average orientation for each axis.

308 The BoxA caliper dimension (Ketcham and Mote 2019), which defines the crystal long
309 axis as the longest axis of the smallest rectangular box that fits the particle, was used for crystal
310 size distribution analyses. Because these measurements were made in 3D, there is no
311 requirement for stereological conversion from 2D to 3D measurements (e.g., Higgins 2000,
312 Morgan and Jerram 2006). CSD plots were created using the same bin sizes for all samples so
313 that direct comparisons can be made. The smallest crystal length from all samples was used for
314 the minimum bin size. Each subsequent bin size is 1.1 times as large as the previous one until the
315 bin size was larger than the largest crystal from all samples. The population density (units of
316 mm^{-4}) was calculated by dividing the number of crystals from each bin size by the volume of
317 sample multiplied by the bin size. Plots of the natural logarithm of the population density versus
318 bin size are commonly used to interpret crystal size distributions. This method is not possible or
319 feasible with other phases in our samples because separating touching and intergrown grains of
320 the same mineral in CT data is not straightforward.

321

322

RESULTS

323 **3D petrographic descriptions**

324 Using CT data for petrographic analyses enables 3D observations of mineral shapes,
325 sizes, orientations, spatial distributions, internal compositional variations, and intergrowths, all
326 of which can be useful for interpreting petrogenesis. Further, CT data can be especially useful for
327 recording other macroscopic textures such as fractures, void spaces, and local melting (Liu et al.
328 2019). Preliminary “hand sample” observations can be made by viewing and manipulating the
329 sample using 3D volume rendering software, and the sample can be digitally sliced along any
330 orthogonal or oblique plane to view internal textures on 2D grayscale images. This is analogous
331 to viewing thousands of back-scattered electron (BSE) images of a serially-sectioned sample cut
332 from all possible angles, but more importantly without processing and physically cutting the
333 sample. In the sections below, we base most of our observations on 2D images obliquely sliced
334 from the 3D data along strategic orientations, e.g., parallel or perpendicular to foliation. Our
335 interpretations are based on what is visible in the studied samples. It is possible that larger or
336 different stones of the same meteorite may differ from ours. Finally, most samples have been
337 meticulously studied previously, and petrographic descriptions on 2D thin sections have been
338 adequate to describe most of the rock textures (see Supplementary Material (Section A)). Thus,
339 we only report new features that have not been recorded or ones that are better studied in 3D.
340

341 *Basaltic and gabbroic*

342 The basaltic (Zagami) and gabbroic (NWA 6963 and NWA 13134) shergottites are
343 predominantly pyroxene and maskelynite with minor high- μ phases (Fig. 1e-g). Zagami has the
344 most abundant pyroxenes (84 %) followed by NWA 6963 (78 %) then NWA 13134 (73 %)
345 (Table 2). Pyroxene crystals are euhedral and create an interlocking structure of elongated prisms
346 with interstitial maskelynite, which takes on a variety of habits, from blocky to elongated to
347 irregular. High- μ phases are euhedral to anhedral with some equant and blocky habits and some
348 with irregular and rounded habits. They are randomly distributed between crystal boundaries.
349 Cross-cutting fractures are present in all samples.

350 Pyroxene crystals, when viewed along a random orientation, have a large range of sizes
351 (from < 1 mm up to 10 mm) and morphologies (from equant and rounded to highly elongated
352 and rod-like). However, when the CT data are strategically oriented along a single crystal's
353 longest, intermediate, and shortest axes, it becomes apparent that pyroxene crystals have a
354 slightly compressed rod-like morphology (Fig. 3). This is true for nearly every crystal in NWA
355 13134 and NWA 6963, whereas a small population of pyroxenes in Zagami are more equant and
356 blocky with sharp edges that meet at approximately 60° and 90°. We are confident the elongated
357 crystals are single, large crystals instead of linked, smaller crystals, because there are small (~50
358 μm thick) bright rims that are three-dimensionally continuous around the entire crystal.
359 Furthermore, fracture spacing, size, and orientation are consistent within a single crystal. Table 3
360 summarizes the length of measured pyroxene crystals. NWA 6963 and NWA 13134 are nearly
361 identical with crystal lengths up to around 13 mm (average = 5.8 mm and 6.4 mm, respectively)
362 and Zagami crystal lengths up to 6.7 mm (average = 2.3 mm). Only crystal lengths were
363 quantified by the rod analysis, but visual observations show that crystal length and diameter
364 scale with one another with NWA 6963 and NWA 13134 crystals up to ~1 mm diameter and
365 Zagami up to ~0.5 mm.
366

367 *Olivine-phyric*

368 Considerable textural diversity exists among the four studied olivine-phyric shergottites
369 (Fig. 1a-d). All are porphyritic with megacrysts of olivine surrounded by a fine- to medium-
370 grained basaltic groundmass of predominantly maskelynite and pyroxene. Samples LAR 12011
371 and Tissint have the most abundant olivine megacrysts (27 % and 26 %, respectively) followed
372 by LAR 12095 (17 %) and EETA 79001 (14 %) (Table 2). Megacryst olivine are up to 4 mm and
373 their morphology/habit vary. Euhedral to subhedral crystals are commonly clustered and
374 touching in samples LAR 12011 and Tissint, whereas olivine in LAR 12095 and EETA 79001
375 are more isolated. LAR 12095 olivine are the most euhedral with flat faces and sharp vertices
376 and edges, whereas many olivines in EETA 79001 have non-linear edges and rounded vertices
377 and reentrant features, although most are still subhedral to euhedral. Olivine in LAR 12095,
378 Tissint, and EETA 79001 have mostly equant dimensions, whereas many of the olivine,
379 especially the larger ones, in LAR 12011 are more tabular.

380 Core-to-rim zoning from lower to higher CT #, which reflects increasing fayalite
381 content, is apparent in large olivine in all samples, with EETA 79001, LAR 12011 and Tissint
382 having well-defined rims that are usually around 50 μm thick) with a higher fayalite content and
383 LAR 12095 having a more subtle increase in fayalite content from core to rim. Zoning is not
384 apparent in the smaller olivine within all samples and they have high CT #'s (i.e., more fayalitic)
385 comparable to the rims of the larger olivine. Olivine-hosted inclusions are common in LAR
386 12095, LAR 12011, and Tissint and rare in EETA 79001. Dark inclusions are interpreted to be
387 melt inclusions and brighter inclusions are interpreted to be primarily oxides (e.g., chromite).
388 Melt inclusions vary from spherical to irregularly shaped and from near the resolution limits of
389 the scan up to several hundred micrometers long. Oxide inclusions are generally equant and
390 about 50 μm long.

391 Groundmass phases are interpreted to be mostly maskelynite and pyroxene with
392 interstitial high- μ phases that are interpreted to be oxides and sulfides. The average abundance of
393 groundmass phases (i.e., pyroxene and maskelynite) is 78 % (range = 72 % to 86 %) (Table 2).
394 Tissint and EETA 79001 have the finest groundmass phases. LAR 12011 has slightly larger
395 groundmass maskelynite with a feathery and elongated morphology and LAR 12095 has the
396 largest groundmass phases with some pyroxene growing up to a few mm long and maskelynite
397 taking on a blocky and more equant habit. Systems of sub-parallel fractures are found in most
398 large olivine but do not propagate into surrounding phases. They are dominantly oriented
399 orthogonally to the crystal long axis. Cross-cutting fractures are found in all samples. A single 2
400 mm x 2 mm shock-melt pocket is found in EETA 79001 based on its unique CT #'s, rounded
401 shape, and internal texture (Fig. 1a – dark circular object in middle of image).

402

403 *Poikilitic*

404 RBT 04261 is a coarse-grained assemblage of poikilitic pyroxenes surrounded by a non-
405 poikilitic groundmass of olivine, pyroxene, and maskelynite (Fig. 1h). The pyroxene oikocrysts
406 are up to 15 mm long and enclose smaller (up to 2 mm) olivine chadacrysts and fine-grained
407 high- μ phases. The non-poikilitic texture contains coarse-grained olivine up to 6 mm long,
408 irregular pyroxene up to 1 mm long, blocky maskelynite (21 %; Table 2), and interstitial high- μ
409 phases. The non-poikilitic olivine are euhedral and form an interlocking framework with
410 interstitial maskelynite. These olivines also have higher fayalite content than the olivine
411 chadacrysts. Zoning is not apparent in either olivine type. Combined (poikilitic and non-
412 poikilitic) olivine and pyroxene abundances are 54 % and 25 %, respectively (Table 2).

413

414 **Modal abundances**

415 Whole-rock and slice-by-slice modal abundances are shown in Fig. 4 and reported in
416 Table 2. We report the whole-rock value and the average, 2σ standard deviation, and Min/Max of
417 the thousands of measured slices and include previously published values for comparison. For
418 each sample, the average of the thousands of measured slices is usually within 1% of the whole-
419 rock value. However, individually, there is significant variation on a slice-by-slice basis,
420 especially for megacryst olivine (up to 31 % in EETA 79001) and pyroxene oikocrysts (up to 26
421 % in RBT 04261). The slice-by-slice variation is less for the basaltic and gabbroic samples. For
422 samples LAR 12095, EETA 79001, and Tissint, the published values are mostly within the total
423 range of slice-by-slice values, whereas the published values are outside this range for Zagami,
424 NWA 6963, and LAR 12011.

425

426 **Petrofabrics**

427 Continuum CT fabric parameters (K and C) of each measured phase (i.e., maskelynite,
428 pyroxene, olivine, and/or high- μ phases) are listed in Table 4 and illustrated on an eigenvalue
429 ratio plot (Woodcock and Naylor 1983) in Fig. 5. On average, basaltic and gabbroic shergottites
430 have the highest fabric strengths (C) (0.59 and 0.62, respectively) followed by the olivine-phyric
431 (0.49) then poikilitic (0.47) shergottites. Most phases display a triaxial (K = 1) to foliated (K < 1)
432 fabric with average K values of 0.64 (basaltic), 0.61 (gabbroic), 0.53 (olivine-phyric), and 0.41
433 (poikilitic). The orientations of continuum fabrics within a single sample are strongly to
434 moderately aligned with respect to one another (Fig. 6 and Table 5). All phases in Zagami, NWA
435 6963, LAR 12095, LAR 12011, and RBT 04261 are strongly aligned (i.e., within 15° of each
436 other) and moderately aligned (i.e., all phases within 25° of each other) in NWA 13134, Tissint,
437 and EETA 79001.

438 The fabric based on discrete pyroxene crystals measured with Blob3D in Zagami, NWA
439 13134, and NWA 6963 indicates foliations similar to the continuum results, but much stronger,
440 with C values higher by a factor of 4 (Figs. 7, S5; Tables 4, S2). NWA 6963 has a nearly uniaxial
441 girdle distribution (i.e., all orientations along the same plane), whereas NWA 13134 and Zagami
442 have around 10 % and 15 %, respectively, of crystals oriented away from the foliation plane.
443 Zagami has a mild preferred orientation within the foliation plane shown by a slight clustering of
444 pyroxene orientations. The pyroxene foliation planes measured with this discrete method
445 generally overlap with the pyroxene continuum measurement; they are within 13.9° of one
446 another in NWA 13134, 20.3° in NWA 6963, and 24.2° in Zagami (Fig. S8). These large
447 differences in fabric strength, and minor differences in orientation, are likely due to a
448 combination of the incomplete sampling of pyroxene crystals for the discrete method and the
449 continuum method merging pyroxene-pyroxene grain boundaries.

450 Like the pyroxene CT fabrics, the high- μ phase discrete fabrics indicate foliations similar
451 to the high- μ phase continuum results, but have more comparable degrees of anisotropy, with C
452 values only higher by a factor of around 1.5 (Fig. S6; Table S1). The high- μ phases' average
453 long, intermediate, and short axis orientations measured with Blob3D (gray data in Fig. 6; Fig
454 S2) are very similar to high- μ Quant3D results. See Supplementary Material (Section J) for a
455 discussion comparing high- μ and pyroxene fabric measurements using Quant3D and Blob3D.

456

457 **Crystal size distributions**

458 Results from 3D crystal size distribution analyses for the high- μ phases are presented in
459 Fig. 8 and Table 6. Between 3,900 and 105,000 individual grains were measured per sample with
460 an average of 24 grains per mm^3 (range 3.8 to 74.3 grains/ mm^3). The basaltic and gabbroic
461 samples have the largest average grain lengths (from 0.12 to 0.26 mm) followed by the poikilitic
462 sample RBT 04261 (0.13 mm) and the olivine-phyric samples (from 0.05 to 0.09 mm). The
463 average ratio of long to short axis (BoxA/BoxC in Table 6) range from 2.18 to 2.41 for the
464 gabbroic and basaltic samples and from 1.73 to 2.03 for the olivine-phyric samples and 1.67 for
465 the poikilitic sample. All samples have a mostly linear and negative CSD slope from their
466 maximum bin size to their turndown bin size. There is a slight increase in slope right before the
467 turndown at smaller bin sizes in all samples except RBT 04261. There is greater deviation from a
468 linear slope at larger bin sizes due to smaller numbers of grains. The steep turndown at the
469 lowest bin sizes is likely a scanning resolution effect as there is a correlation ($r^2 = 0.83$) between
470 the scanning voxel size and the turndown bin size (Fig. S3), which is around four times as large
471 as the voxel size (slope = 0.27). The shortest axis (BoxC) is the controlling factor for visibility in
472 the CT data, which is usually around half the length of the longest axis (BoxA), implying that the
473 thinnest axis length where grains are beginning to be excluded from measurement is around two
474 voxels. We only use the values greater than the turndowns for linear regressions and interpreting
475 CSD patterns because data in bin sizes below the respective turndowns are likely to be in part a
476 resolution effect and not a petrogenetic feature.

477 Distinctly different CSD patterns correlate with lithology. The basaltic and gabbroic
478 samples have shallower slopes (-8 to -3 mm^{-1}) and extend to larger bin sizes (1.3 to 3.5 mm),
479 especially NWA 13134 and NWA 6963, which are nearly indistinguishable. The latter two have
480 a slight increase in slope at around 0.3 mm sizes before the turndowns. The olivine-phyric
481 samples have steeper slopes (-34 to -11 mm^{-1}) and smaller maximum sizes (<0.76 mm). LAR
482 12095, LAR 12011, and Tissint are nearly linear from the largest bin sizes down to the turndown
483 bin sizes, whereas EETA 79001 is linear from the largest bin sizes to around 0.24 mm and
484 slightly concave up from 0.24 mm to the turndown bin size. The poikilitic sample has a slope of $-$
485 12 mm^{-1} and a maximum bin size of 1.0 mm with a highly linear ($r^2 = 1.00$) CSD pattern down to
486 its turndown bin size.

488 **DISCUSSION**

489 **Implications of grain-scale heterogeneity**

490 The importance of measuring whole-rock versus slice-by-slice modal abundances is
491 illustrated in Figs. 4 and 9 and Table 2. The average modal abundance measured on thousands of
492 slices per sample is within $\sim 1\%$ of the whole-rock value, but any single slice can vary
493 significantly from the whole-rock modal abundance. This is especially true for samples with
494 isolated phases that are significantly larger than groundmass phases (e.g., phenocrysts). The
495 likelihood of olivine megacryst or pyroxene oikocryst abundance on a random slice being $\pm 1 \%$
496 of the whole volume value decreases from 33.9 % (LAR 12011) to 20.9 % (Tissint) to 17.5 %
497 (RBT 04261) to 17.0 % (LAR 12095) to 10.8 % (EETA 79001). Similarly, the 2RSD (relative
498 standard deviation) for megacryst phase abundance on the thousands of CT slices increases from
499 16.5 % (LAR 12011) to 30.5 % (Tissint) to 39.7 % (RBT 04261) to 60.5% (LAR 12095) to
500 105.5% (EETA 79001).

501 This divergence has significant implications when classifying samples and allocating
502 “representative” thin/thick sections or aliquots for petrological/geochemical analyses. Initial

503 meteorite classifications are sometimes based on observations from a single section. Fig. 9 shows
504 the minimum and maximum modal abundances of olivine megacrysts and pyroxene oikocrysts
505 that can be observed on a single slice from the same samples. For instance, if the minimum
506 olivine megacryst slice for EETA 79001 was sectioned for classification, this sample would be
507 classified as a basaltic lithology, and not olivine-phyric. Similarly, there are no intact pyroxene
508 oikocrysts in the minimum abundance slice for RBT 04261. Based on this slice, RBT 04261
509 would be classified as an olivine cumulate with little pyroxene. While it is unlikely to randomly
510 cut the sample on a plane with the minimum or maximum value for a specific phase, for a
511 sample like EETA 79001, which has a high megacryst 2RSD (>100%) and a low likelihood
512 (~10%) of a random slice being $\pm 1\%$ of the whole volume average, there is a higher likelihood
513 of misinterpreting the lithology from a single slice. Based on our results, the samples we studied
514 are accurately classified. However, new samples, or volumetrically small samples where as few
515 as one thin section can be made, would benefit from being classified using X-ray CT.
516 Additionally, CT scanning can allow a specific plane to be selected for sectioning (e.g., Hanna et
517 al. 2015), or a representative and contextualized volume of sample be allocated for
518 geochemical/isotopic analyses via dissolution. For instance, the olivine megacrysts are evenly
519 distributed throughout LAR 12011, so a random volume from this sample should be
520 representative. However, the distribution of olivine megacrysts in LAR 12095, EETA 79001, and
521 Tissint is heterogeneous, requiring a larger volume of rock to obtain a similarly representative
522 aliquot.

523

524 **Relative cooling rates from CSD analysis**

525 There are distinct interstitial high- μ CSD patterns for the basaltic, gabbroic, olivine-
526 phyric, and poikilitic lithologies. For the gabbroic and basaltic samples, it is interesting that
527 NWA 6963 and NWA 13134 have almost identical CSD patterns. Based on this and other
528 textural similarities (i.e., pyroxene sizes and modal abundances), NWA 13134 might be paired
529 with NWA 6963. NWA 13134 is a relatively new and unstudied sample (Burney et al. 2022), so
530 future geochemical and/or geochronological work may confirm this pairing. Extending this high-
531 μ CSD method to additional shergottites may prove to be a relatively quick and quantitative tool
532 for lithologic classification and possibly aid in defining meteorite pairing groups.

533 Effective application of CSD theory requires that every crystal from a specific mineral
534 group (e.g., all pyroxenes or all olivines) is individually measured within a sample. The
535 interstitial high- μ phases measured here are interpreted to be both oxides and sulfides, which
536 have been commonly reported as interstitial opaque minerals in other petrographic studies and
537 are some of the last phases to crystallize (Barrat et al. 2002, Gattacceca et al. 2013, Goodrich
538 2003, Herd et al. 2002, Herd et al. 2001, McCoy et al. 1992, Sarbadhikari et al. 2009). These
539 authors found that pyrrhotite are smaller (<20 μm) and less abundant (<1 %) than the interstitial
540 oxides (1 – 2 %), which are dominantly titanomagnetite and also include subordinate abundances
541 of ilmenite. While we cannot distinguish between the sulfides and oxides in the CT data,
542 previous investigations indicate that most sulfides are likely within bin sizes below the CSD
543 turndowns. A small population of the relatively larger sulfides added to the oxides in bin sizes
544 near the turndown might be the cause of the slight increase in slope near the turndown.
545 Therefore, the CSD patterns reflect mixing of different but overlapping mineral size classes.
546 However, due to the sulfides' small sizes, the patterns most likely reflect the growth of oxides,
547 mainly titanomagnetite.

548 Most shergottite CSD analyses are of olivine and/or pyroxene with the goal of
549 understanding: (1) physical processes within the parent magma such as crystal accumulation or
550 fractionation; (2) crystal growth rates; (3) residence times; and (4) nucleation histories (Ennis
551 and McSween 2014, Filiberto et al. 2018, Lentz and McSween 2000, Rahib et al. 2019). The goal
552 of our high- μ CSD analyses is to understand the final stages of crystallization as interstitial
553 oxides are some of the last phases to form. If we assume the high- μ phases and growth rates are
554 the same in all samples, the steeper CSD slopes are interpreted to reflect a shorter residence time
555 (i.e., faster cooling rate during parent melt solidification). To calculate residence times, the
556 crystal growth rate must be known and assumed to be constant. The generally linear form of the
557 CSD patterns is consistent with a constant growth rate under steady-state conditions.
558 Unfortunately, there have been no experiments measuring growth rates of titanomagnetite in
559 shergottitic melts, thus, quantifying residence times is not possible. However, we can infer
560 relative differences in residence times. The gabbroic samples (NWA 6963 and NWA 13134) had
561 the most prolonged crystallization period, followed by Zagami (basaltic) and RBT 04261
562 (poikilitic), then by the olivine-phyric samples (LAR 12011, LAR 12095, EETA 79001, and
563 Tissint). This interpretation is consistent with other groundmass mineral grain sizes with the
564 gabbroic samples being the coarsest followed by the basaltic and poikilitic samples then the
565 olivine-phyric samples. These results cannot be used to infer the specific solidification
566 environment for each sample but are useful for determining relative differences in cooling rates
567 during the final period of crystallization.

568

569 **Interpreting fabrics**

570 Continuum and discrete fabric analyses revealed that most phases preserve a foliated to
571 triaxial fabric and that CT fabrics of multiple phases measured within a single sample are
572 strongly to moderately aligned. Generally, foliated igneous fabrics are interpreted to form in
573 environments where the principal forces are normal to the foliation plane with limited simple
574 shear, possibly from compaction in a thicker lava flow or settling/compression in a sub-volcanic
575 sill, dike, or chamber (Meurer and Boudreau 1998, Nicolas et al. 2009). Simple shear, which is
576 the dominant deformation regime in lava flows, is expected to impart a foliation with a preferred
577 orientation (Iezzi and Ventura 2002, Merle 2000, Reed and Tryggvason 1974). However, a
578 complementary analogue study of CT fabrics in terrestrial mafic rocks with various geologic
579 contexts (dikes, sills, flows, and lava lakes) shows there is no correlation between the CT fabric
580 parameters and solidification environment because of several factors intrinsic to an individual
581 sample and extrinsic ones related to the magma itself (Eckley 2022). Interestingly, they do show
582 that the only samples ($n = 3$) with strong degrees of CT fabric alignment are from shallow
583 intrusive environments (i.e., dikes and sills) where the principal stresses associated with magma
584 emplacement in some dikes or sills may be more constant and uniformly align phases whereas
585 extrusive flows tend to be more chaotic during flow and solidification.

586 Comparing our CT fabric results to the analogue study by Eckley (2022) is complicated
587 by differences in minerals and their abundances and shapes, degrees of aggregation, and
588 presence and coalescence of vesicles, among other factors. However, we still posit that shear
589 forces are more consistent in subsurface emplacement environments than within lava flows on
590 Mars, which uniformly aligned the measured CT fabrics. It may also be possible that phases can
591 become strongly aligned at the base of lava flows, especially thicker ones, but we do not yet have
592 data to test this hypothesis. Therefore, we interpret the strong to moderate degrees of CT fabric

593 alignment in the samples from this study to reflect uniform and consistent principal forces during
594 solidification, most likely in subsurface environments.

595 Additional evidence for a subsurface emplacement environment for the basaltic and
596 gabbroic samples is borne out by the fabric analysis of individual pyroxene crystals. Pyroxene
597 crystals in gabbroic samples (NWA 13134 and NWA 6963) are almost exclusively large and rod-
598 like and show a strongly foliated fabric with no preferred orientation. We interpret this fabric to
599 have likely formed from the settling, accumulation, and compaction of pyroxene crystals in a
600 subsurface magma chamber with no simple shear component (i.e., flow). Most of the pyroxene
601 crystals in the basaltic sample (Zagami) are also rod-like but have a slightly weaker pyroxene
602 foliation and a mild preferred orientation within the foliation plane. This fabric suggests there
603 was a mild component of simple shear during solidification, most likely from directional forces
604 associated with flow.

605

606 **Models for shergottite emplacement**

607 Here we describe models for the emplacement of shergottites in this study inferred from
608 both the petrofabric analyses and high- μ phase crystal size distribution analyses in the context of
609 previous studies.

610

611 *Gabbroic*

612 The coarse-grained nature of the gabbroic shergottites (NWA 13134 and NWA 6963) is
613 interpreted to reflect an emplacement environment with slower cooling rates compared to other
614 groups. This interpretation has been reiterated by Udry et al. (2017) for NWA 7320 through
615 geochemical and petrological analyses and by Filiberto et al. (2018) through geochemical,
616 petrological, and quantitative 2D textural analyses of pyroxene in NWA 6963. Filiberto et al.
617 (2018) interpreted their CSD plots to reflect accumulation of crystals with relatively long
618 residence times. Interestingly, the CSD*slice* (Morgan and Jerram 2006) software used in their
619 study, which is commonly used to stereologically predict 3D shapes from 2D data, matched a
620 rectangular prism habit with an aspect ratio of 1.00:1.20:1.90 and a maximum length of around
621 3.25 mm. When viewed in 3D along strategic orientations, the pyroxene in NWA 6963 are rod-
622 like with highly anisotropic aspect ratios (1.00:1.60:20.00 for the pyroxene in Fig. 3) and an
623 average length of 5.8 mm (up to 13 mm). Their work followed the standard procedure for 2D
624 CSD analyses, but caution should be taken when measuring samples like NWA 6963 that have
625 highly anisotropic crystal habits. While the thin/thick section making process is often out of the
626 analyst's control, a single, random 2D thin section may not be adequate for accurate CSD
627 analyses and to identify rod-like shapes or other 3D shapes. A section oriented along the foliation
628 plane (Figs. 10-column B and S9-left) would provide a more realistic representation of the rock.
629 Similarly, the 2D pyroxene shape preferred orientation (SPO) analyses resulted in a dominantly
630 clustered distribution, which is certainly an artifact of their section not being parallel to the
631 foliation plane. Nevertheless, based on their combined quantitative textural and geochemical
632 analyses, they infer that NWA 6963 was emplaced as a cumulate rock in the Martian subsurface.
633 Our results corroborate this interpretation. All evidence (relatively long late-stage residence time
634 from high- μ CSD analyses and a strongly foliated fabric of large and rod-like pyroxene crystals)
635 points toward emplacement in a subsurface environment with settling and accumulation of
636 pyroxene and no flow component, likely in a sill or magma chamber, for NWA 6963 and NWA
637 13134.

638

639 *Basaltic*

640 Zagami has long been recognized as having a relatively slow cooling rate during the final
641 crystallization period when compared to other basaltic and olivine-phyric shergottites (Becker et
642 al. 2011, McCoy et al. 1992, Stolper and McSween 1979). This was inferred from its coarse-
643 grained nature, high crystal abundance, and thick pyroxene exsolution lamellae. They
644 hypothesized that these conditions are achievable in a thick (> 10 m) lava flow or thin intrusive
645 environment. Stolper and McSween (1979) and Becker et al. (2011) measured foliated pyroxene
646 SPO and crystallographic preferred orientation (CPO), respectively, and inferred that Zagami
647 formed in an intrusive cumulate environment with no directional flow. McCoy et al. (1992)
648 measured a similar foliated pyroxene SPO but stated that without confirmation of a lineation
649 associated with the foliation, then a cumulate environment is not substantiated. Here we confirm
650 that there is a foliated pyroxene SPO but with a mild preferred orientation along the foliation
651 plane. However, this may not indicate crystallization in a thick lava flow as injection of a magma
652 into a dike may impart a flow direction component onto the rock fabric. The strong alignment of
653 CT fabrics in Zagami also suggests solidification in an environment where principal forces align
654 all phases similarly. Again, Eckley (2022) shows that alignment of phases does happen in a
655 subsurface environment but hypothesize it may also occur in a thick lava flow. The final line of
656 evidence against eruption to the surface and solidification as a lava flow is the high pyroxene
657 abundance (84%), which is drastically higher than the critical crystallinity (~55%) that prevents a
658 basaltic magma from erupting and flowing (Marsh 1981). Therefore, we propose that Zagami
659 formed in an intrusive body, possibly injected as a dike, at a shallower depth, or in a smaller
660 volume magma body, than the gabbroic shergottites.

661
662 *Poikilitic*

663 Poikilitic sample RBT 04261 is hypothesized to have been emplaced in an environment
664 with relatively slow cooling rates, likely in a hypabyssal cumulate environment. This
665 interpretation is based on quantitative 2D textural analyses of the non-poikilitic olivine in RBT
666 04261 and several other poikilitic shergottites (Combs et al. 2019, Howarth et al. 2014, Rahib et
667 al. 2019, Udry et al. 2020) that show accumulation of the non-poikilitic olivine. The strong
668 alignment of CT fabrics and high crystal content (olivine + pyroxene oikocrysts = 78 %)
669 measured here are consistent with emplacement in a subsurface cumulate environment. Based on
670 similar high- μ CSD patterns, RBT 04261 may have been emplaced at temperature and pressure
671 conditions similar to Zagami.

672
673 *Olivine-phyric*

674 The olivine-phyric shergottites have the finest-grained groundmass minerals and high- μ
675 CSD patterns which both reflect the quickest cooling rates during solidification. Olivine-phyric
676 shergottite Yamato 980459 is inferred to have erupted and quenched in a thin lava flow based on
677 its high abundance of glassy mesostasis (Usui et al. 2008) and dynamic crystallization
678 experiments (First and Hammer 2016). Aside from Yamato 980459, most shergottites are simply
679 interpreted to have experienced a relatively high cooling rate during the final period of
680 crystallization based on their fine-grained groundmass minerals and distinct Fe-rich olivine rims
681 (Dunham et al. 2019, Ennis and McSween 2014, Liu et al. 2013, Liu et al. 2016, Sarbadhikari et
682 al. 2009, Udry et al. 2020). Such a cooling rate is not only achievable during extrusion as a lava
683 flow, but also during emplacement of shallow intrusives (i.e., dikes and sills). Chilled margins,
684 quenched textures, and Fe-rich olivine rims are all common in terrestrial basaltic dikes and sills

685 (Petcovic and Dufek 2005). Balta et al. (2015) reported highly evolved late-stage minerals (Ti-
686 rich oxides, Fe-rich olivine, and Fe-rich merrillite) in Tissint that required a prolonged cooling
687 during the final stages of crystallization. They infer that slow final cooling requires emplacement
688 in a sill or dike rather than eruption at the surface. Here we show that LAR 12011, LAR 12095,
689 EETA 79001, and Tissint all have strong to moderately aligned CT fabrics which we interpret as
690 having formed during emplacement into a shallow intrusive environment, likely dikes and/or
691 sills that are possibly associated with a volcanic edifice. The depth of emplacement is unknown,
692 but at shallower depths, and/or in thinner magma bodies, than the gabbroic, poikilitic, and
693 basaltic shergottites in this study.

694

695 **Implications of subsurface emplacement**

696 Determining where within the martian crust shergottites finally crystallized has broad
697 implications for better understanding possible sources of syn- and post-emplacement
698 modification, remote sensing observations, and the growth and evolution of martian volcanic
699 centers. Prolonged crystallization at depth versus rapid quenching at the surface vary
700 significantly in the amount of time the rock spent at elevated subsolidus temperatures. This can
701 have drastic effects on the thermally-activated diffusion of rapidly-diffusing elements (e.g. H, Li,
702 Be, B) whose in-situ geochemical profiles have been used to infer possible volatile outgassing
703 (Lentz et al. 2001, Udry et al. 2016) or presence of primordial volatile reservoirs using volatiles
704 in glasses from mineral-hosted melt inclusions (Gross et al. 2013a, Usui et al. 2012) or in
705 volatile-bearing minerals like apatite (Filiberto et al. 2016, Gross et al. 2013a, McCubbin et al.
706 2016, McCubbin et al. 2012). Shergottites that experienced rapid cooling are likely to be less
707 affected by thermally-activated diffusion, making interpretations of their geochemical profiles
708 more robust.

709 While shergottites represent only a small and selective portion of the martian crust, they
710 are useful to help understand some remote sensing observations. For instance, McSween et al.
711 (2006) identified similarities between Gusev crater rocks and olivine-phyric rocks. Since olivine-
712 phyric shergottites are more likely to have been emplaced closer to the surface when compared
713 to other shergottites in this study, this could provide an explanation for a high abundance of
714 olivine at the surface. Given the ancient ages of the Gusev crater olivine-rich rocks (~3.65 Ga
715 (Greeley et al. 2005)) compared to the much younger shergottite ages (~165-600 Ma (Borg et al.
716 2003, Brennecka et al. 2014, Nyquist et al. 2001, Váci and Agee 2020)) this could imply a
717 tendency for solidification of olivine-rich samples in near surface environments on Mars over a
718 wide span of geologic time. Determining the solidification environments of shergottites is a
719 crucial step in trying to give these rocks geologic context.

720 Finally, the samples in this study are a small but representative suite spanning the
721 dominant lithological and geochemical categories. Extending the analyses we presented here to a
722 statistically significant number of samples with various crystallization ages, ejection ages, and
723 geochemical signatures may provide an opportunity to understand the crystallization conditions
724 of individual volcanic systems on Mars. For instance, Lapen et al. (2017) identified a suite of
725 shergottites (n = 11) with the same ejection age and mantle source signature, but with
726 crystallization ages from 348 Ma to 2.4 Ga, suggesting the presence of a long-lived volcanic
727 center. A systematic petrofabric analysis of such a suite of samples could provide insight into
728 how volcanic centers have grown and evolved on Mars.

729

730

CONCLUSIONS

731 The analysis of 3D petrofabrics and crystal size distributions in shergottites using X-ray
732 computed tomography provides valuable insights into their final moments of crystallization,
733 which reflect the environments in which these martian igneous rocks solidified. We used a 3D
734 star volume distribution method to measure the strength, type, and direction of shape preferred
735 orientation of the phases (i.e., maskelynite, pyroxene, olivine, and/or oxides/sulfides) within
736 eight shergottite meteorites covering the known lithologic and geochemical subcategories. Most
737 phases preserve a foliated to triaxial petrofabric with variable degrees of anisotropy. Five out of
738 eight samples have strongly aligned petrofabrics where the eigenvector orientations for the
739 different phases within a sample are aligned to within 15° of each other, and the other three
740 samples have moderately aligned petrofabrics. This alignment is likely caused by uniform
741 stresses during solidification, which may be common in intrusive environments. These results
742 indicate that the samples in this study were probably emplaced in the subsurface, either as
743 cumulates or shallow intrusives. Measurements of individual pyroxene crystal orientations
744 provide further refinement of emplacement models for the gabbroic and basaltic shergottites in
745 this study. Gabbroic shergottites were emplaced in a subsurface cumulate environment with no
746 flow, possibly a large sill or magma chamber, whereas the basaltic shergottite was emplaced in a
747 subsurface environment with a minor flow component, possibly injected as a dike. The crystal
748 size distribution patterns of interstitial oxides and sulfides are unique for the different lithologic
749 types and reflect relative differences in cooling rates between different sample types during the
750 final stages of crystallization. Together, these results are used to evaluate the solidification
751 environments of the samples from this study. Gabbroic (NWA 6963 and NWA 13134), basaltic
752 (Zagami), and poikilitic (RBT 04261) shergottites were emplaced in the subsurface with
753 gabbroic samples solidifying at deeper depths, or in larger magma bodies. Olivine-phyric
754 shergottites (LAR 12011, LAR 12095, EETA 79001, and Tissint) were also emplaced in the
755 subsurface but as shallower intrusive bodies such as dikes or sills. The degree of geochemical
756 enrichment or depletion of each sample did not correlate directly to a sample's petrofabric or
757 emplacement as enriched shergottites existed across the full range of emplacement modes
758 identified in this study. The absence of such a correlation between cooling history, depth of
759 emplacement, and degree of geochemical enrichment is consistent with the idea that the source
760 of enrichment within the enriched shergottites may not be, solely, the martian crust (Barnes et al.
761 2020, Brandon et al. 2012, Sarbadhikari et al. 2009, Sarbadhikari et al. 2011, Shearer et al. 2013,
762 Tait and Day 2018). Subsurface emplacement histories have important implications for
763 understanding the interaction of shergottite melts with upper crustal materials, cooling histories,
764 and remote sensing observations.

765 766 **ACKNOWLEDGEMENTS**

767 We thank the Astromaterials X-ray Fluorescence and Computed Tomography (X-FaCT)
768 Lab at NASA – Johnson Space center, the University of Texas High-Resolution X-ray Computed
769 Tomography Lab (UTCT), and the Analysis and Test Laboratory at NASA – Jet Propulsion
770 Laboratory for the collection of X-ray CT data. We thank Linda Welzenbach and Marc Fries for
771 loaning a sample of Tissint. US Antarctic meteorite samples are recovered by the Antarctic
772 Search for Meteorites (ANSMET) program which has been funded by NSF and NASA, and
773 characterized and curated by the Department of Mineral Sciences of the Smithsonian Institution
774 and Astromaterials Acquisition and Curation office (AACO) at NASA Johnson Space Center.
775 The CT data for RBT 04261 were produced for the Astromaterials 3D project in NASA's
776 Acquisition & Curation Office and were funded by NASA Planetary Data Archiving,

777 Restoration, and Tools Program, Proposal No.: 15-PDART15_2-0041. The CT data for NWA
778 13134 and YL's participation in this project was supported partially by NASA award
779 80NM0018F0612 and by internal grants at Jet Propulsion Laboratory, which is managed by
780 Caltech under a contract with NASA. UTCT is partially supported through NSF-IF grant EAR-
781 2223808 and NASA 22-PSEF22_2-0018 to RAK. The authors also thank Gopalan Srinivasan,
782 for editorial handling, and two anonymous reviewers.

783

784

DATA AVAILABILITY

785 The data that support the findings of this study are available in the supplementary
786 material of this article which is openly available in a Mendeley Data Repository (DOI:
787 10.17632/mzgp37947y.1).

788

789

CONFLICT OF INTERESTS

790 The authors declare that they have no known competing financial interests or personal
791 relationships that could have appeared to influence the work reported in this paper.

792

793

REFERENCES

794

- 795 Balta, J. B., M. E. Sanborn, A. Udry, M. Wadhwa, and H. Y. McSween. 2015. Petrology and
796 trace element geochemistry of Tissint, the newest shergottite fall. *Meteoritics &*
797 *Planetary Science* 50 (1):63-85.
- 798 Barnes, J. J., F. M. McCubbin, A. R. Santos, J. M. Day, J. W. Boyce, S. P. Schwenzer, U. Ott, I.
799 A. Franchi, S. Messenger, and M. Anand. 2020. Multiple early-formed water reservoirs
800 in the interior of Mars. *Nature Geoscience* 13 (4):260-264.
- 801 Barrat, J., P. Gillet, V. Sautter, A. Jambon, M. Javoy, C. Göpel, M. Lesourd, F. Keller, and E.
802 Petit. 2002. Petrology and chemistry of the basaltic shergottite North West Africa 480.
803 *Meteoritics & Planetary Science* 37 (4):487-499.
- 804 Becker, T., V. Reynolds, R. Beane, and T. McCoy. 2011. Preferred orientations of pyroxene in
805 the Zagami shergottite: Implications for magmatic emplacement. 42nd Annual Lunar and
806 Planetary Science Conference.
- 807 Blumenfeld, E., K. Beaulieu, A. Thomas, C. Evans, R. Zeigler, E. Oshel, D. Liddle, K. Righter,
808 R. Hanna, and R. Ketcham. 2019. 3D Virtual Astromaterials Samples Collection of
809 NASA'S Apollo Lunar and Antarctic Meteorite Samples to be an Online Database to
810 Serve Researchers and the Public. Lunar and Planetary Science Conference.
- 811 Borg, L. E., and D. S. Draper. 2003. A petrogenetic model for the origin and compositional
812 variation of the Martian basaltic meteorites. *Meteoritics & Planetary Science* 38
813 (12):1713-1731.
- 814 Borg, L. E., L. E. Nyquist, H. Wiesmann, C.-Y. Shih, and Y. Reese. 2003. The age of Dar al
815 Gani 476 and the differentiation history of the martian meteorites inferred from their
816 radiogenic isotopic systematics. *Geochimica et Cosmochimica Acta* 67 (18):3519-3536.
- 817 Brandon, A. D., I. S. Puchtel, R. J. Walker, J. M. Day, A. J. Irving, and L. A. Taylor. 2012.
818 Evolution of the martian mantle inferred from the 187Re-187Os isotope and highly
819 siderophile element abundance systematics of shergottite meteorites. *Geochimica et*
820 *Cosmochimica Acta* 76:206-235.
- 821 Brennecka, G., L. Borg, and M. Wadhwa. 2014. Insights into the Martian mantle: The age and
822 isotopics of the meteorite fall Tissint. *Meteoritics & Planetary Science* 49 (3):412-418.

823 Burney, D., Y. Liu, M. Kipp, J. Eiler, F. Tissot, and K. Farley. 2022. A New Martian Gabbroic
824 Shergottite, Northwest Africa (NWA) 13134. *Lunar and Planetary Science Conference*.
825 Abstract#: 2530.

826 Cardozo, N., and R. W. Allmendinger. 2013. Spherical projections with OSXStereonet.
827 *Computers & Geosciences* 51:193-205.

828 Combs, L. M., A. Udry, G. H. Howarth, M. Righter, T. J. Lapen, J. Gross, D. K. Ross, R. R.
829 Rahib, and J. M. Day. 2019. Petrology of the enriched poikilitic shergottite Northwest
830 Africa 10169: Insight into the martian interior. *Geochimica et Cosmochimica Acta*
831 266:435-462.

832 Crisp, J. A. 1984. Rates of magma emplacement and volcanic output. *Journal of Volcanology*
833 *and Geothermal Research* 20 (3-4):177-211.

834 Duke, M. B. 1968. The Shergotty meteorite: Magmatic and shock metamorphic features. *Shock*
835 *metamorphism of natural materials*.:613-621.

836 Dunham, E. T., J. B. Balta, M. Wadhwa, T. G. Sharp, and H. Y. McSween Jr. 2019. Petrology
837 and geochemistry of olivine-phyric shergottites LAR 12095 and LAR 12240:
838 Implications for their petrogenetic history on Mars. *Meteoritics & planetary science* 54
839 (4):811-835.

840 Eckley, S. A. 2022. Magmatic thermal histories and emplacement mechanisms of Martian
841 shergottite meteorites. Ph.D., University of Texas at Austin.

842 Ennis, M. E., and H. Y. McSween. 2014. Crystallization kinetics of olivine-phyric shergottites.
843 *Meteoritics & Planetary Science* 49 (8):1440-1455.

844 Filiberto, J., J. Gross, and F. M. McCubbin. 2016. Constraints on the water, chlorine, and
845 fluorine content of the Martian mantle. *Meteoritics & Planetary Science* 51 (11):2023-
846 2035.

847 Filiberto, J., J. Gross, A. Udry, J. Trela, A. Wittmann, K. M. Cannon, S. Penniston-Dorland, R.
848 Ash, V. E. Hamilton, and A. L. Meado. 2018. Shergottite Northwest Africa 6963: A
849 Pyroxene-Cumulate Martian Gabbro. *Journal of Geophysical Research: Planets* 123
850 (7):1823-1841.

851 First, E., and J. Hammer. 2016. Igneous cooling history of olivine-phyric shergottite Yamato
852 980459 constrained by dynamic crystallization experiments. *Meteoritics & Planetary*
853 *Science* 51 (7):1233-1255.

854 Fisher, N. I., T. Lewis, and B. J. Embleton. 1993. *Statistical analysis of spherical data*:
855 Cambridge university press.

856 Gattacceca, J., R. H. Hewins, J. P. Lorand, P. Rochette, F. Lagroix, C. Cournède, M. Uehara, S.
857 Pont, V. Sautter, and R. B. Scorzelli. 2013. Opaque minerals, magnetic properties, and
858 paleomagnetism of the Tissint Martian meteorite. *Meteoritics & Planetary Science* 48
859 (10):1919-1936.

860 Gattacceca, J., F. M. McCubbin, J. N. Grossman, D. L. Schrader, N. L. Chabot, M. D'orazio, C.
861 Goodrich, A. Greshake, J. Gross, and K. H. Joy. 2023. The Meteoritical Bulletin, No.
862 111. *Meteoritics & Planetary Science*.

863 Goodrich, C. A. 2003. Petrogenesis of olivine-phyric shergottites Sayh al Uhaymir 005 and
864 Elephant Moraine A79001 lithology A. *Geochimica et Cosmochimica Acta* 67
865 (19):3735-3772.

866 Greeley, R., B. H. Foing, H. Y. McSween Jr, G. Neukum, P. Pinet, M. van Kan, S. C. Werner, D.
867 A. Williams, and T. E. Zegers. 2005. Fluid lava flows in Gusev crater, Mars. *Journal of*
868 *Geophysical Research: Planets* 110 (E5).

869 Greshake, A., J. Fritz, and D. Stöffler. 2004. Petrology and shock metamorphism of the olivine-
870 phyric shergottite Yamato 980459: Evidence for a two-stage cooling and a single-stage
871 ejection history. *Geochimica et Cosmochimica Acta* 68 (10):2359-2377.

872 Griffin, S., L. Daly, T. Keller, S. Piazzolo, L. V. Forman, M. R. Lee, R. J. Baumgartner, P. W.
873 Trimby, G. K. Benedix, A. J. Irving, and B. Hoefnagels. 2022. Constraints on the
874 emplacement of martian Nakhilite igneous rocks and their source volcano from advanced
875 petrofabric analysis. *Journal of Geophysical Research: Planets* 127 (6); e2021JE007080.

876 Gross, J., J. Filiberto, and A. S. Bell. 2013a. Water in the martian interior: Evidence for
877 terrestrial MORB mantle-like volatile contents from hydroxyl-rich apatite in olivine-
878 phyric shergottite NWA 6234. *Earth and Planetary Science Letters* 369:120-128.

879 Gross, J., J. Filiberto, C. D. Herd, M. M. Daswani, S. P. Schwenzer, and A. H. Treiman. 2013b.
880 Petrography, mineral chemistry, and crystallization history of olivine-phyric shergottite
881 NWA 6234: A new melt composition. *Meteoritics & Planetary Science* 48 (5):854-871.

882 Gross, J., A. H. Treiman, J. Filiberto, and C. D. Herd. 2011. Primitive olivine-phyric shergottite
883 NWA 5789: Petrography, mineral chemistry, and cooling history imply a magma similar
884 to Yamato-980459. *Meteoritics & Planetary Science* 46 (1):116-133.

885 Hanna, R. D., and R. A. Ketcham. 2017. X-ray computed tomography of planetary materials: A
886 primer and review of recent studies. *Chemie der Erde-Geochemistry* 77 (4):547-572.

887 Hanna, R. D., R. A. Ketcham, M. Zolensky, and W. M. Behr. 2015. Impact-induced brittle
888 deformation, porosity loss, and aqueous alteration in the Murchison CM chondrite.
889 *Geochimica et Cosmochimica Acta* 171:256-282.

890 Herd, C. D., L. E. Borg, J. H. Jones, and J. J. Papike. 2002. Oxygen fugacity and geochemical
891 variations in the Martian basalts: Implications for Martian basalt petrogenesis and the
892 oxidation state of the upper mantle of Mars. *Geochimica et Cosmochimica Acta* 66
893 (11):2025-2036.

894 Herd, C. D., J. J. Papike, and A. J. Brearley. 2001. Oxygen fugacity of martian basalts from
895 electron microprobe oxygen and TEM-EELS analyses of Fe-Ti oxides. *American
896 Mineralogist* 86 (9):1015-1024.

897 Higgins, M. D. 2000. Measurement of crystal size distributions. *American Mineralogist* 85
898 (9):1105-1116.

899 Howarth, G. H., J. F. Pernet-Fisher, J. B. Balta, P. H. Barry, R. J. Bodnar, and L. A. Taylor.
900 2014. Two-stage polybaric formation of the new enriched, pyroxene-oikocrystic,
901 lherzolitic shergottite, NWA 7397. *Meteoritics & Planetary Science* 49 (10):1812-1830.

902 Iezzi, G., and G. Ventura. 2002. Crystal fabric evolution in lava flows: results from numerical
903 simulations. *Earth and Planetary Science Letters* 200 (1-2):33-46.

904 Ketcham, R., and A. Mote. 2019. Accurate measurement of small features in X-ray CT data
905 volumes, demonstrated using gold grains. *Journal of Geophysical Research: Solid Earth*.

906 Ketcham, R., and T. M. Ryan. 2004. Quantification and visualization of anisotropy in trabecular
907 bone. *Journal of microscopy* 213 (2):158-171.

908 Ketcham, R. A. 2005a. Computational methods for quantitative analysis of three-dimensional
909 features in geological specimens. *Geosphere* 1 (1):32-41.

910 Ketcham, R. A. 2005b. Three-dimensional grain fabric measurements using high-resolution X-
911 ray computed tomography. *Journal of Structural Geology* 27 (7):1217-1228.

912 Ketcham, R. A., and W. D. Carlson. 2001. Acquisition, optimization and interpretation of X-ray
913 computed tomographic imagery: applications to the geosciences. *Computers &
914 Geosciences* 27 (4):381-400.

- 915 Lapen, T. J., M. Richter, R. Andreasen, A. J. Irving, A. M. Satkoski, B. L. Beard, K. Nishiizumi,
916 A. J. T. Jull, and M. W. Caffee. 2017. Two billion years of magmatism recorded from a
917 single Mars meteorite ejection site. *Science Advances* 3(2): e1600922.
- 918 Lentz, R., H. McSween, J. Ryan, and L. Riciputi. 2001. Water in martian magmas: clues from
919 light lithophile elements in shergottite and nakhlite pyroxenes. *Geochimica et*
920 *Cosmochimica Acta* 65 (24):4551-4565.
- 921 Lentz, R., and H. Y. McSween. 2000. Crystallization of the basaltic shergottites: Insights from
922 crystal size distribution (CSD) analysis of pyroxenes. *Meteoritics & Planetary Science*
923 35 (5):919-927.
- 924 Liu, Y., J. B. Balta, C. A. Goodrich, H. Y. McSween Jr, and L. A. Taylor. 2013. New constraints
925 on the formation of shergottite Elephant Moraine 79001 lithology A. *Geochimica et*
926 *Cosmochimica Acta* 108:1-20.
- 927 Liu, Y., I. P. Baziotis, P. D. Asimow, R. J. Bodnar, and L. A. Taylor. 2016. Mineral chemistry of
928 the Tissint meteorite: Indications of two-stage crystallization in a closed system.
929 *Meteoritics & Planetary Science* 51 (12):2293-2315.
- 930 Liu, Y., S. Eckley, and E. Blumenfeld. 2019. Most Shergottites were Once Vesicular: Evidence
931 from 3D Computed X-Ray Tomography. 82nd Annual Meeting of The Meteoritical
932 Society.
- 933 Marsh, B. 1981. On the crystallinity, probability of occurrence, and rheology of lava and magma.
934 *Contributions to Mineralogy and Petrology* 78 (1):85-98.
- 935 McCoy, T. J., G. J. Taylor, and K. Keil. 1992. Zagami: Product of a two-stage magmatic history.
936 *Geochimica et Cosmochimica Acta* 56 (9):3571-3582.
- 937 McCubbin, F. M., J. W. Boyce, P. Srinivasan, A. R. Santos, S. M. Elardo, J. Filiberto, A. Steele,
938 and C. K. Shearer. 2016. Heterogeneous distribution of H₂O in the Martian interior:
939 Implications for the abundance of H₂O in depleted and enriched mantle sources.
940 *Meteoritics & Planetary Science* 51 (11):2036-2060.
- 941 McCubbin, F. M., E. H. Hauri, S. M. Elardo, K. E. Vander Kaaden, J. Wang, and C. K. Shearer
942 Jr. 2012. Hydrous melting of the martian mantle produced both depleted and enriched
943 shergottites. *Geology* 40 (8):683-686.
- 944 McSween, H., and A. Treiman. 1998. Planetary Materials. *Reviews in Mineralogy* 36:6-1-6-54.
- 945 McSween, H. Y. 2015. Petrology on Mars. *American Mineralogist* 100 (11-12):2380-2395.
- 946 Mcsween, H. Y., D. D. Eisenhour, L. A. Taylor, M. Wadhwa, and G. Crozaz. 1996. QUE94201
947 shergottite: Crystallization of a Martian basaltic magma. *Geochimica et Cosmochimica*
948 *Acta* 60 (22):4563-4569.
- 949 McSween, H. Y., M. B. Wyatt, R. Gellert, J. Bell, R. V. Morris, K. E. Herkenhoff, L. S.
950 Crumpler, K. A. Milam, K. R. Stockstill, and L. L. Tornabene. 2006. Characterization
951 and petrologic interpretation of olivine-rich basalts at Gusev Crater, Mars. *Journal of*
952 *Geophysical Research: Planets* 111 (E2).
- 953 Merle, O. 2000. Numerical modelling of strain in lava tubes. *Bulletin of volcanology* 62 (1):53-
954 58.
- 955 Meurer, W., and A. Boudreau. 1998. Compaction of igneous cumulates part II: compaction and
956 the development of igneous foliations. *The Journal of Geology* 106 (3):293-304.
- 957 Morgan, D. J., and D. A. Jerram. 2006. On estimating crystal shape for crystal size distribution
958 analysis. *Journal of Volcanology and Geothermal Research* 154 (1-2):1-7.

- 959 Moser, D., K. Chamberlain, K. Tait, A. Schmitt, J. R. Darling, I. Barker, and B. Hyde. 2013.
960 Solving the Martian meteorite age conundrum using micro-baddeleyite and launch-
961 generated zircon. *Nature* 499 (7459):454-457.
- 962 Nicolas, A., F. Boudier, and L. France. 2009. Subsidence in magma chamber and the
963 development of magmatic foliation in Oman ophiolite gabbros. *Earth and Planetary
964 Science Letters* 284 (1-2):76-87.
- 965 Nyquist, L., D. Bogard, C.-Y. Shih, A. Greshake, D. Stöffler, and O. Eugster. 2001. Ages and
966 geologic histories of Martian meteorites. In *Chronology and evolution of Mars*, 105-164.
967 Springer.
- 968 Orr, K. J., L. V. Forman, K. Rankenburg, N. J. Evans, B. J. McDonald, B. Godel, and G. K.
969 Benedix. 2022. Geochemical and mineralogical classification of four new shergottites:
970 NWA 10441, NWA 10818, NWA 11043, and NWA 12335. *Meteoritics & Planetary
971 Science* 57 (6): 1194-1223.
- 972 Petcovic, H. L., and J. D. Dufek. 2005. Modeling magma flow and cooling in dikes: Implications
973 for emplacement of Columbia River flood basalts. *Journal of Geophysical Research:
974 Solid Earth* 110 (B10).
- 975 Rahib, R. R., A. Udry, G. H. Howarth, J. Gross, M. Paquet, L. M. Combs, D. L. Laczniak, and J.
976 M. Day. 2019. Mantle source to near-surface emplacement of enriched and intermediate
977 poikilitic shergottites in Mars. *Geochimica et Cosmochimica Acta* 266:463-496.
- 978 Reed, L. J., and E. Tryggvason. 1974. Preferred orientations of rigid particles in a viscous matrix
979 deformed by pure shear and simple shear. *Tectonophysics* 24 (1-2):85-98.
- 980 Sarbadhikari, A. B., J. M. Day, Y. Liu, D. Rumble III, and L. A. Taylor. 2009. Petrogenesis of
981 olivine-phyric shergottite Larkman Nunatak 06319: Implications for enriched
982 components in Martian basalts. *Geochimica et Cosmochimica Acta* 73 (7):2190-2214.
- 983 Sarbadhikari, A. B., C. A. Goodrich, Y. Liu, J. M. Day, and L. A. Taylor. 2011. Evidence for
984 heterogeneous enriched shergottite mantle sources in Mars from olivine-hosted melt
985 inclusions in Larkman Nunatak 06319. *Geochimica et Cosmochimica Acta* 75 (22):6803-
986 6820.
- 987 Shearer, C., P. Aaron, P. Burger, Y. Guan, A. Bell, and J. Papike. 2013. Petrogenetic linkages
988 among fO₂, isotopic enrichments-depletions and crystallization history in Martian
989 basalts. Evidence from the distribution of phosphorus in olivine megacrysts. *Geochimica
990 et Cosmochimica Acta* 120:17-38.
- 991 Shearer, C., P. Burger, J. Papike, F. McCubbin, and A. Bell. 2015. Crystal chemistry of merrillite
992 from Martian meteorites: Mineralogical recorders of magmatic processes and planetary
993 differentiation. *Meteoritics & Planetary Science* 50 (4):649-673.
- 994 Smith, J., and R. Hervig. 1979. Shergotty meteorite: Mineralogy, petrography and minor
995 elements. *Meteoritics* 14 (1):121-142.
- 996 Staddon, L. G., J. R. Darling, W. H. Schwarz, N. R. Stephen, S. Schuindt, J. Dunlop, and K. T.
997 Tait. 2021. Dating martian mafic crust; microstructurally constrained baddeleyite
998 geochronology of enriched shergottites Northwest Africa (NWA) 7257, NWA 8679 and
999 Zagami. *Geochimica et Cosmochimica Acta* 315:73-88.
- 1000 Stolper, E., and H. Y. McSween. 1979. Petrology and origin of the shergottite meteorites.
1001 *Geochimica et Cosmochimica Acta* 43 (9):1475-1498.
- 1002 Tait, K. T., and J. M. Day. 2018. Chondritic late accretion to Mars and the nature of shergottite
1003 reservoirs. *Earth and Planetary Science Letters* 494:99-108.

- 1004 Tibaldi, A. 2015. Structure of volcano plumbing systems: A review of multi-parametric effects.
1005 *Journal of Volcanology and Geothermal Research* 298:85-135.
- 1006 Udry, A., G. H. Howarth, C. Herd, J. M. Day, T. J. Lapen, and J. Filiberto. 2020. What martian
1007 meteorites reveal about the interior and surface of Mars. *Journal of Geophysical*
1008 *Research: Planets* 125 (12):e2020JE006523.
- 1009 Udry, A., G. H. Howarth, T. J. Lapen, and M. Righter. 2017. Petrogenesis of the NWA 7320
1010 enriched martian gabbroic shergottite: Insight into the martian crust. *Geochimica et*
1011 *Cosmochimica Acta* 204:1-18.
- 1012 Udry, A., H. Y. McSween Jr, R. L. Hervig, and L. A. Taylor. 2016. Lithium isotopes and light
1013 lithophile element abundances in shergottites: Evidence for both magmatic degassing and
1014 subsolidus diffusion. *Meteoritics & Planetary Science* 51 (1):80-104.
- 1015 Usui, T., C. M. D. Alexander, J. Wang, J. I. Simon, and J. H. Jones. 2012. Origin of water and
1016 mantle–crust interactions on Mars inferred from hydrogen isotopes and volatile element
1017 abundances of olivine-hosted melt inclusions of primitive shergottites. *Earth and*
1018 *Planetary Science Letters* 357:119-129.
- 1019 Usui, T., H. Y. McSween Jr, and C. Floss. 2008. Petrogenesis of olivine-phyric shergottite
1020 Yamato 980459, revisited. *Geochimica et Cosmochimica Acta* 72 (6):1711-1730.
- 1021 Usui, T., M. Sanborn, M. Wadhwa, and H. Y. McSween Jr. 2010. Petrology and trace element
1022 geochemistry of Robert Massif 04261 and 04262 meteorites, the first examples of
1023 geochemically enriched lherzolithic shergottites. *Geochimica et Cosmochimica Acta* 74
1024 (24):7283-7306.
- 1025 Váci, Z., and C. Agee. 2020. Constraints on martian chronology from meteorites. *Geosciences*
1026 10 (11):455.
- 1027 Wenzel, A., J. Filiberto, N. Stephen, S. P. Schwenzer, and S. J. Hammond. 2021. Constraints on
1028 the petrologic history of gabbroic shergottite Northwest Africa 6963 from pyroxene
1029 zoning profiles and electron backscattered diffraction. *Meteoritics & Planetary Science*
1030 56 (9):1744-1757.
- 1031 Woodcock, N., and M. A. Naylor. 1983. Randomness testing in three-dimensional orientation
1032 data. *Journal of Structural Geology* 5 (5):539-548.

1033

1034
1035
1036
1037

TABLES

Table 1: CT scanning facilities and conditions

Sample	Facility	X-ray energy (kV)	X-ray power (W)	Beam filtering	Exposure (s)	Projections	Frame averaging	Voxel size (μm)	Dimensions (voxels)
Zagami NWA	JSC	90	3.0	none	2.83	3141	2	11.49	1708 x 1436 x 1071
13134 NWA 6963	JPL JSC	170 100	7.7 3.0	none 0.1 mm Cu	0.64 1.42	2305 2121	8 2	10.70 18.03	2737 x 2716 x 1792 1200 x 1134 x 2000
LAR 12095	JSC	95	3.0	0.1 mm Al	2.00	2521	2	8.57	1634 x 1396 x 1360
LAR 12011 EETA	JSC	95	3.0	0.1 mm Al	2.00	2831	4	12.49	1364 x 1456 x 1140
79001	JSC	95	3.0	0.1 mm Al	2.00	3141	4	13.14	1362 x 1590 x 775
Tissint	JSC	95	3.0	0.1 mm Al	2.00	1891	2	12.69	836 x 979 x 1622
RBT 04261	UTCT	190	34.0	Al	1.00	3000	2	19.40	1494 x 1589 x 1880

1038
1039

1040
1041

Table 2: Whole-rock and slice-by-slice modal abundances

Sample/Phase	Whole-rock Abundances	Individual Slice Abundances				
		Mean	(2 σ)	Min.	Max.	# of Slices
Zagami						
Maskelynite	14.0	14.0	2.3	11.0	19.0	2453
Pyroxene	83.7	83.7	2.3	78.7	86.9	
High- μ	2.3	2.3	0.5	1.3	3.1	
NWA 13134						
Maskelynite	23.7	23.6	3.5	18.5	29.2	2353
Pyroxene	73.3	73.4	3.3	68.1	78.1	
High- μ	3.0	3.0	0.7	2.0	4.8	
NWA 6963						
Maskelynite	19.9	20.1	3.8	14.5	28.4	2653
Pyroxene	78.2	78.0	3.6	70.3	83.7	
High- μ	1.9	1.9	0.5	0.7	2.8	
LAR 12095						
Maskelynite	15.9	15.8	3.2	11.4	21.0	2753
Pyroxene	66.0	65.6	8.6	52.3	76.0	
Megacrysts	17.3	17.7	10.7	6.7	33.8	
High- μ	0.8	0.8	0.4	0.4	1.6	
LAR 12011						
Maskelynite	10.0	9.9	1.6	7.7	14.2	2428
Pyroxene	62.1	62.1	4.0	57.0	67.5	
Megacrysts	27.3	27.3	4.5	21.8	32.7	
High- μ	0.6	0.6	0.2	0.4	1.1	
EETA 79001						
Maskelynite	13.9	14.1	4.0	8.1	19.2	2003
Pyroxene	72.2	72.7	11.2	58.4	83.2	
Megacrysts	13.5	12.8	13.5	0.0	30.9	
High- μ	0.4	0.4	0.3	0.0	1.0	
Tissint						
Maskelynite	13.2	13.3	2.1	10.8	18.1	2333
Pyroxene	60.2	60.5	6.5	49.5	70.7	
Megacrysts	25.9	25.5	7.8	13.2	38.5	
High- μ	0.7	0.7	0.2	0.3	1.1	
RBT 04261						
Maskelynite	20.6	21.0	3.5	13.2	26.6	3603
Pyroxene	24.8	23.9	9.5	11.1	37.1	
Olivine	53.6	54.3	8.3	44.9	66.0	
High- μ	1.0	1.0	0.3	0.6	1.7	

1042
1043

1044 **Table 3:** Length of pyroxene long axis from Blob3D analysis
1045

Sample	Pyroxene Long Axis (mm)				Count
	Average	1sd	Min	Max	
Zagami NWA	2.3	1.2	0.6	6.7	121
13134	6.4	2.4	1.8	13.1	110
NWA 6963	5.8	2.4	0.7	13.0	117

1046

1047

1048

1049
1050

Table 4: Continuum CT fabric shape parameters, K and C, from Quant3D analysis

Sample/Phase	K	1σ	C	1σ
Zagami				
<i>Maskelynite</i>	0.96	0.13	0.71	0.04
<i>Pyroxene</i>	0.51	0.09	0.49	0.03
<i>High-μ</i>	0.44	0.08	0.57	0.03
NWA 13134				
<i>Maskelynite</i>	0.54	0.10	0.57	0.03
<i>Pyroxene</i>	0.25	0.05	0.65	0.03
<i>High-μ</i>	0.42	0.09	0.46	0.03
NWA 6963				
<i>Maskelynite</i>	1.26	0.17	0.57	0.03
<i>Pyroxene</i>	0.93	0.12	0.86	0.04
<i>High-μ</i>	0.28	0.06	0.61	0.04
LAR 12095				
<i>Maskelynite</i>	0.23	0.08	0.40	0.03
<i>Pyroxene</i>	0.13	0.05	0.38	0.02
<i>Olivine</i>	0.91	0.10	0.70	0.03
<i>High-μ</i>	0.19	0.08	0.37	0.03
LAR 12011				
<i>Maskelynite</i>	0.96	0.15	0.64	0.04
<i>Pyroxene</i>	0.12	0.05	0.57	0.03
<i>Olivine</i>	0.20	0.05	1.26	0.06
<i>High-μ</i>	0.15	0.06	0.50	0.04
EETA 79001				
<i>Maskelynite</i>	1.38	0.46	0.28	0.03
<i>Pyroxene</i>	0.42	0.13	0.19	0.01
<i>High-μ</i>	0.22	0.06	0.34	0.02
Tissint				
<i>Maskelynite</i>	0.62	0.14	0.43	0.04
<i>Pyroxene</i>	0.29	0.09	0.31	0.02
<i>Olivine</i>	1.01	0.17	0.54	0.03
<i>High-μ</i>	1.06	0.17	0.37	0.03
RBT 04261				
<i>Maskelynite</i>	0.46	0.09	0.56	0.02
<i>Olivine</i>	0.56	0.07	0.44	0.03
<i>High-μ</i>	0.21	0.07	0.41	0.02

1051

1052 **Table 5:** Angle between CT fabric orientations (°)

1053

Sample	Maskelynite - Pyroxene	Maskelynite - Olivine	Maskelynite - High-μ	Pyroxene - Olivine	Pyroxene - High-μ	Olivine - High-μ
Zagami	8.6		2.0		10.5	
NWA 13134	11.3		16.9		23.4	
NWA 6963	8.7		7.5		4.8	
LAR 12095	4.9	6.5	8.0	9.2	11.6	6.8
LAR 12011	8.9	12.7	14.3	5.9	6.6	6.4
Tissint	12.2	20.4	12.9	11.7	2.8	11.8
EETA 79001	22.9		18.6		8.9	
RBT 04261		8.6	8.3			9.6

1054

1055 **Table 6:** High- μ phase crystal size distribution analysis results

1056

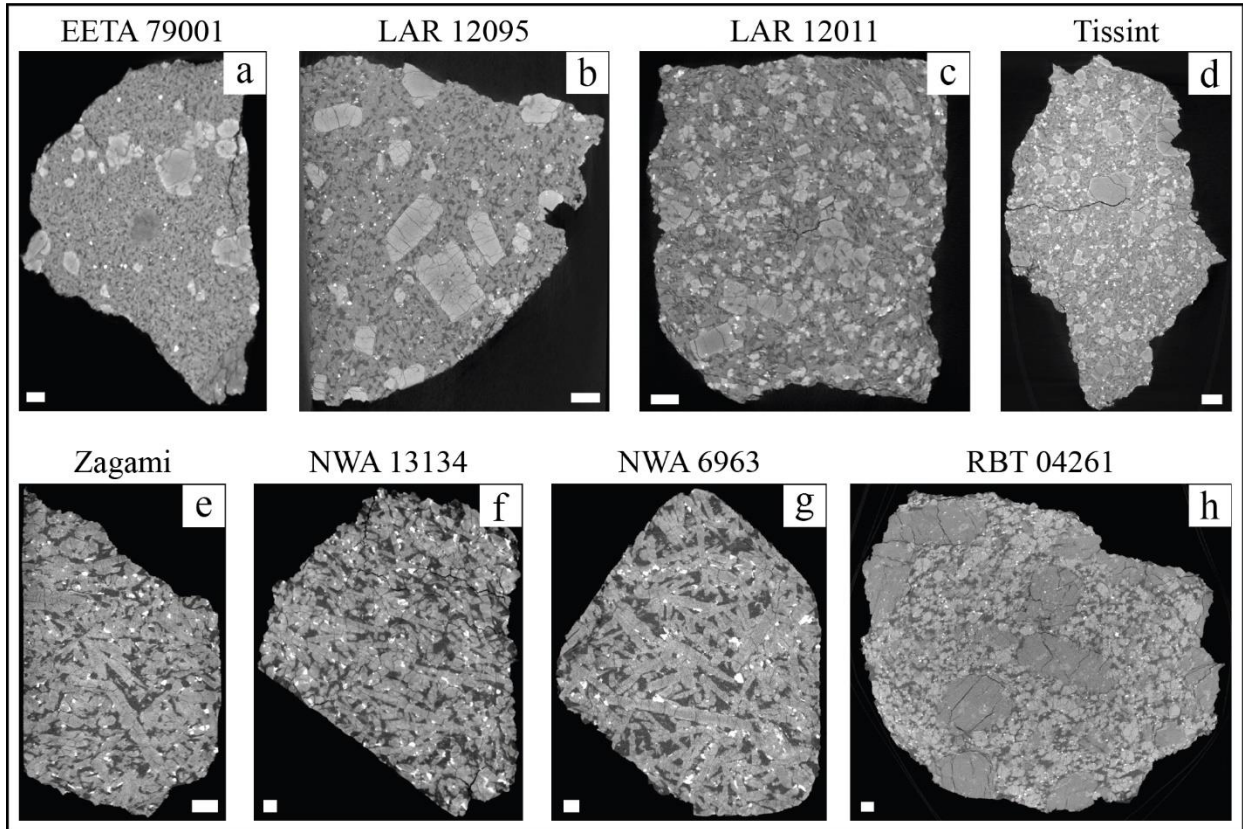
Sample	# of Grains	Measured Volume (mm ³)	Average Length (mm)	± 1 SD (mm)	BoxA/BoxC	± 1 SD	Bin Interval	Slope (mm ⁻¹)	Y-intercept	R ²
Zagami	16336	858	0.12	0.11	2.41	0.92	0.04 - 1.34	-7.95	5.18	0.98
NWA 13134	17357	4564	0.26	0.25	2.18	0.79	0.07 - 3.48	-3.27	2.59	0.97
NWA 6963	17639	3335	0.22	0.22	2.32	0.85	0.06 - 2.87	-3.86	3.14	0.97
LAR 12095	23877	322	0.05	0.04	1.73	0.51	0.03 - 0.52	-21.16	7.60	0.97
LAR 12011	12348	1039	0.06	0.03	2.03	0.86	0.04 - 0.32	-33.51	7.23	0.99
EETA 79001	3874	450	0.09	0.07	1.92	0.69	0.06 - 0.76	-11.19	4.74	0.94
Tissint	41028	705	0.07	0.05	1.83	0.60	0.04 - 0.63	-18.59	7.51	0.99
RBT 04261	105233	11348	0.13	0.08	1.67	0.61	0.06 - 1.01	-11.77	5.31	1.00

1057

1058
1059
1060
1061
1062
1063

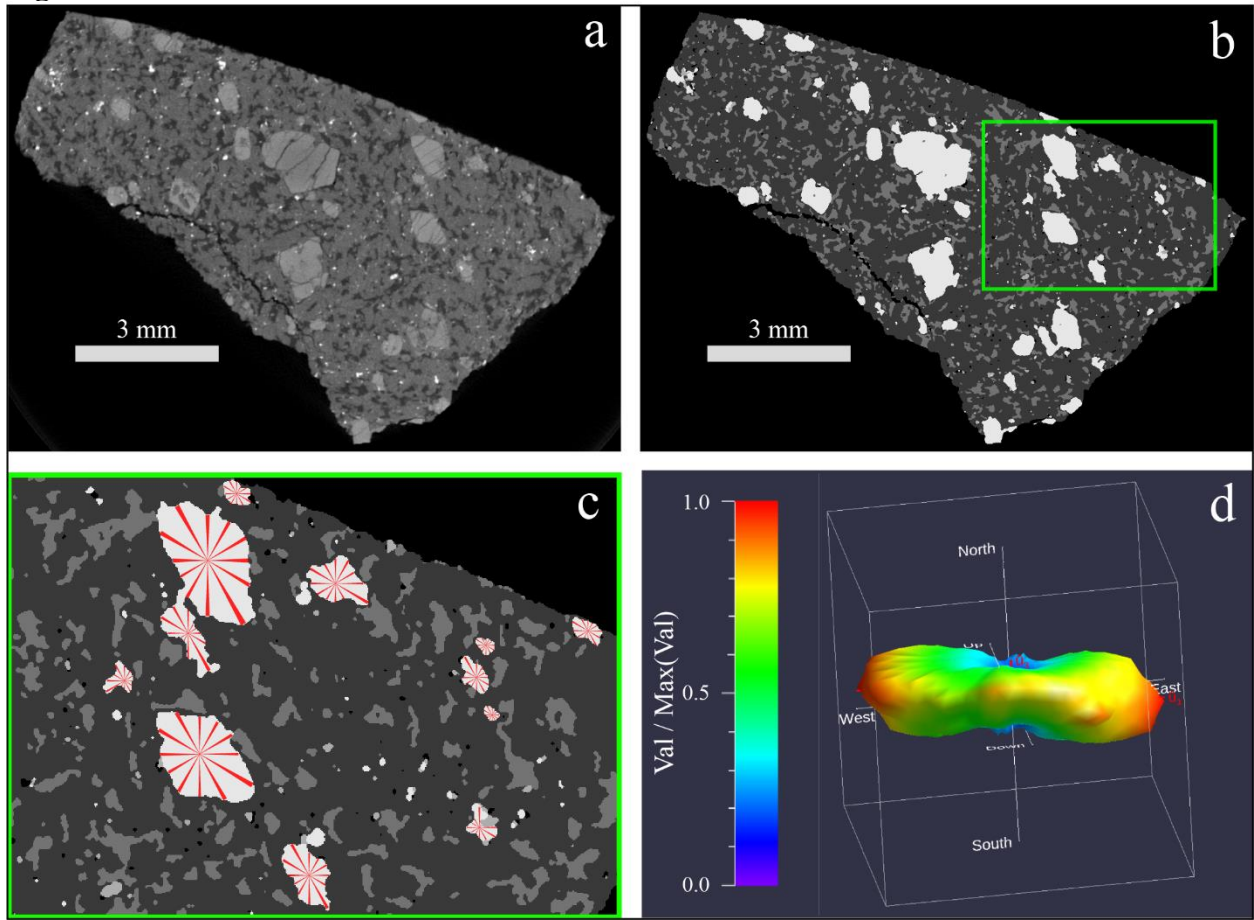
FIGURES

Figure 1



1064
1065

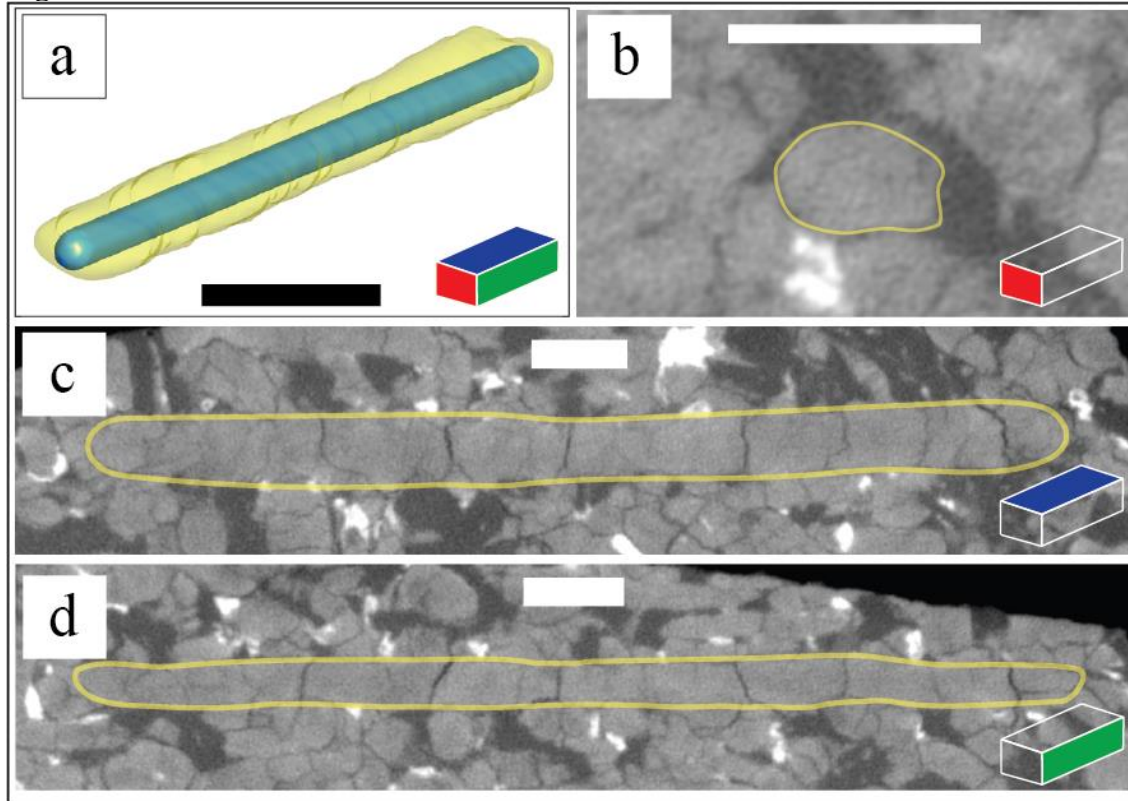
1066 **Figure 2**



1067
1068
1069
1070
1071
1072
1073
1074

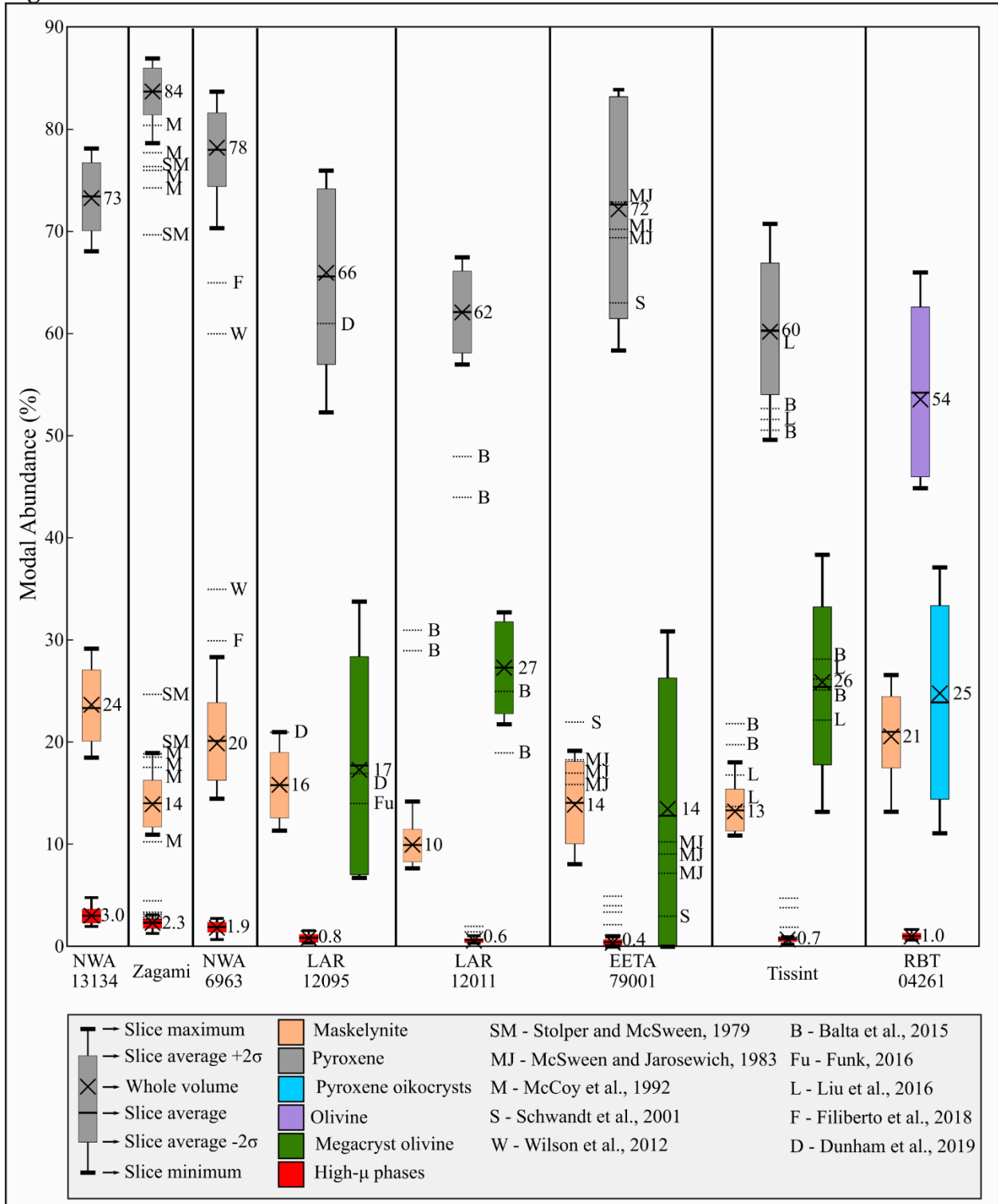
1075

Figure 3

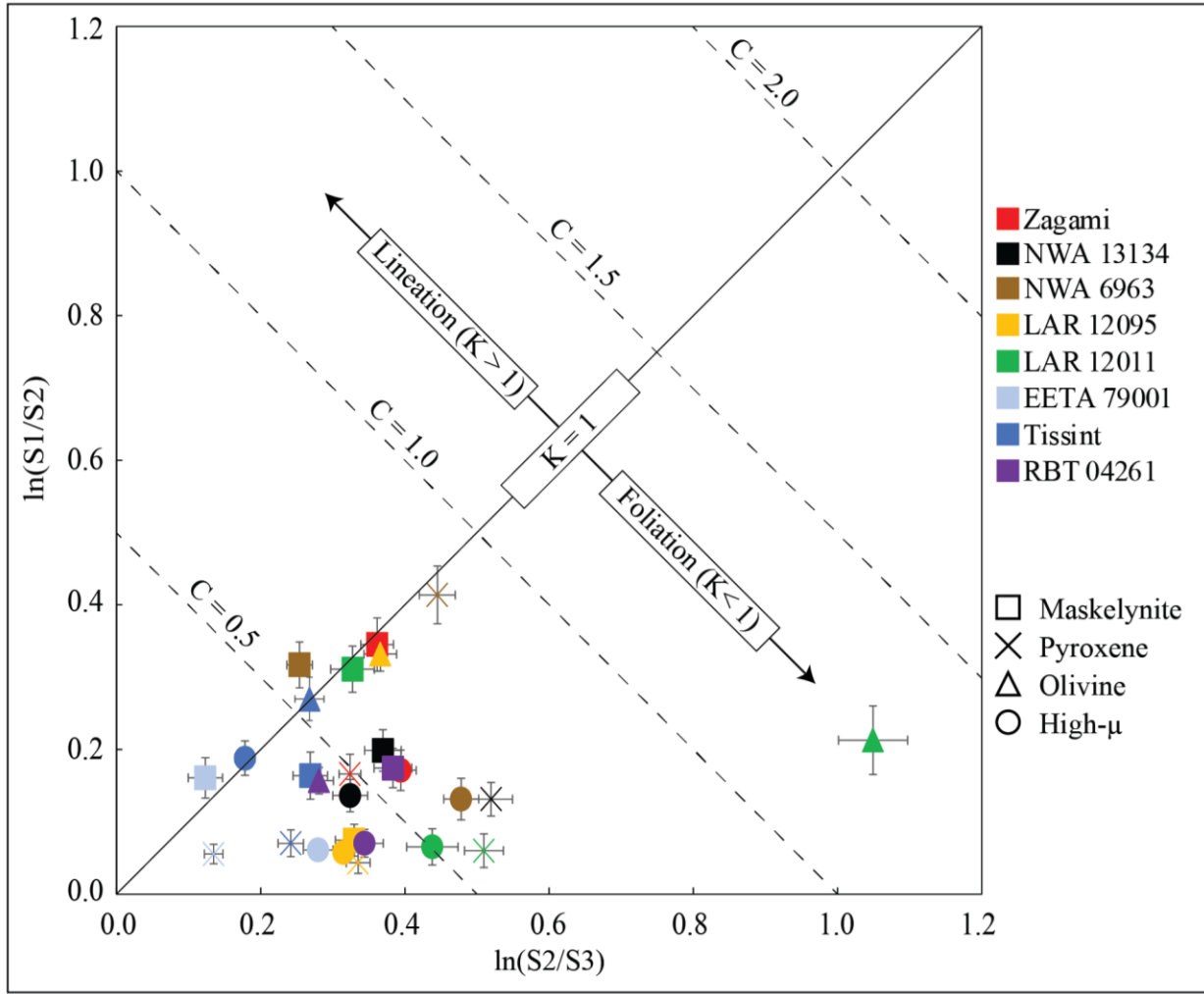


1076
1077

Figure 4



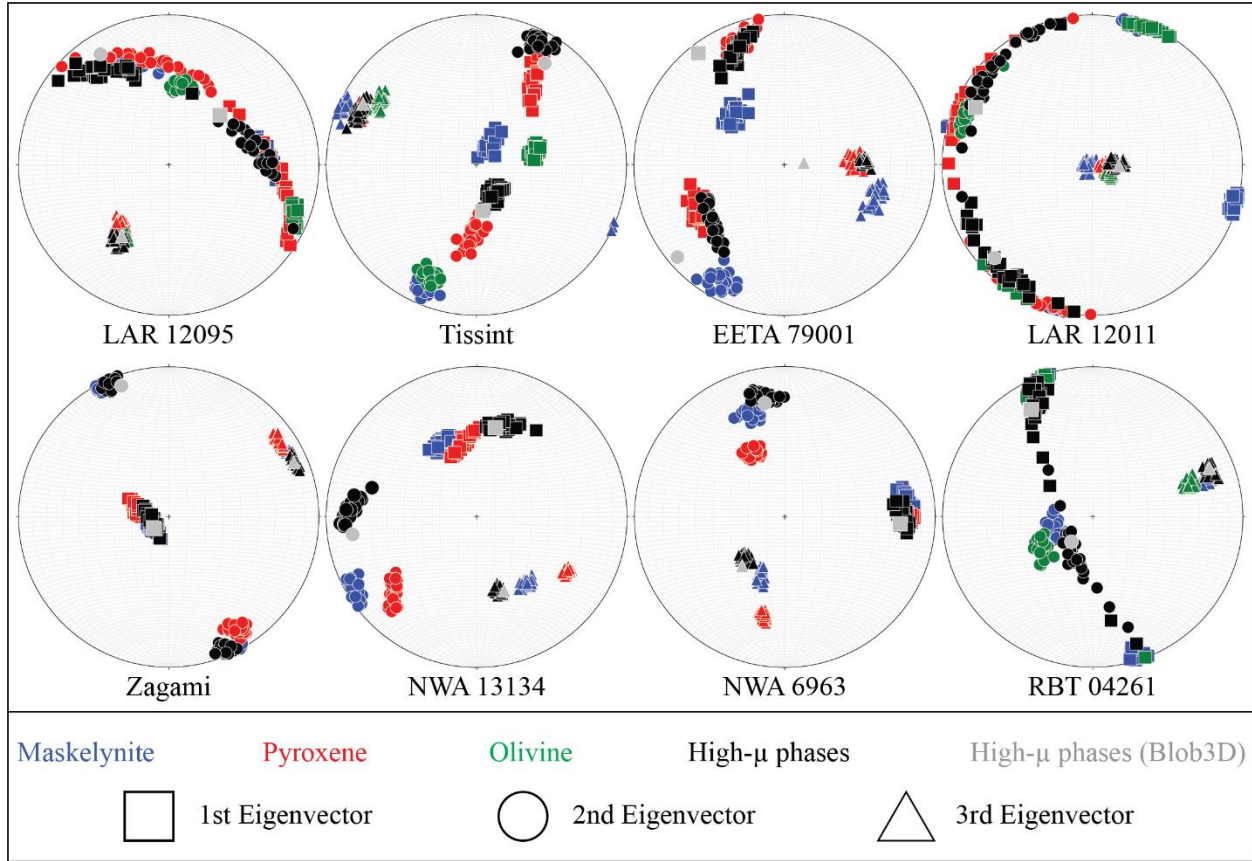
1080 **Figure 5**



1081
1082

1083
1084

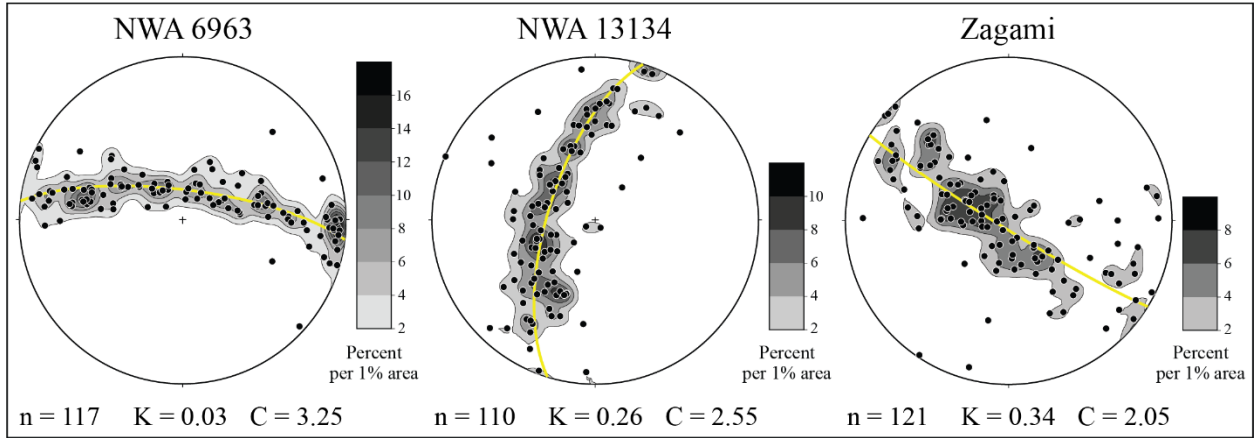
Figure 6



1085

1086
1087

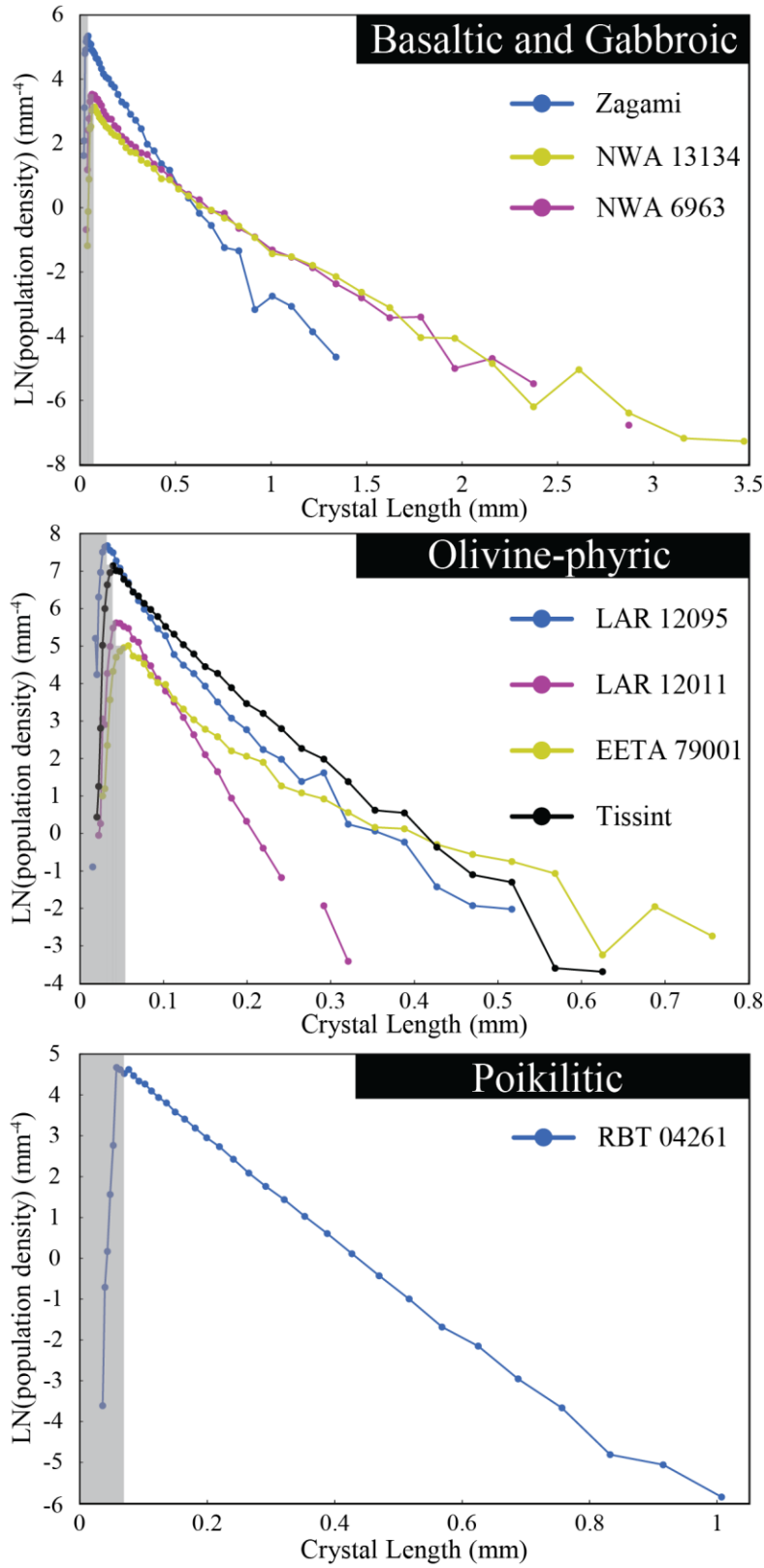
Figure 7



1088

1089
1090

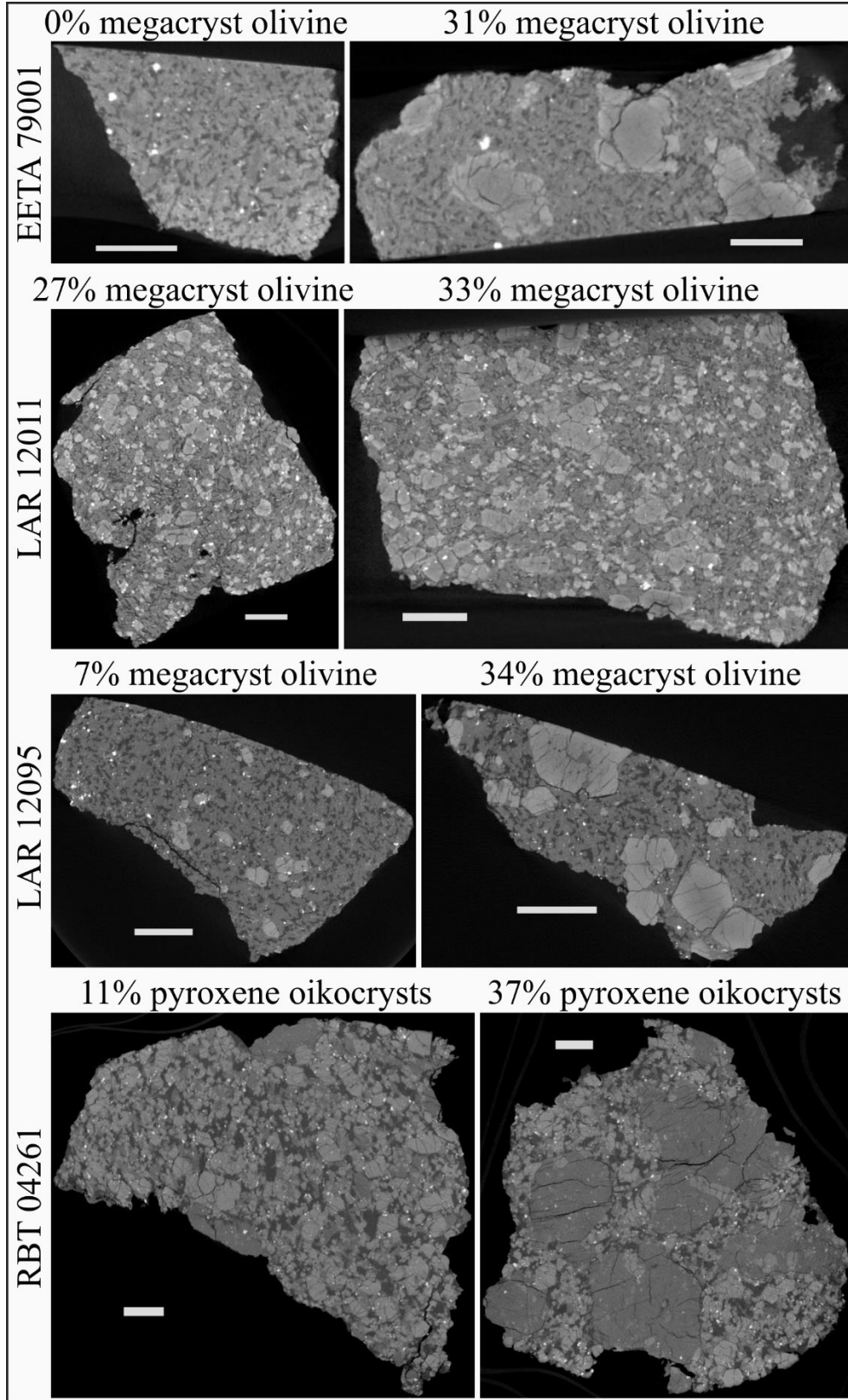
Figure 8



1091

1092
1093

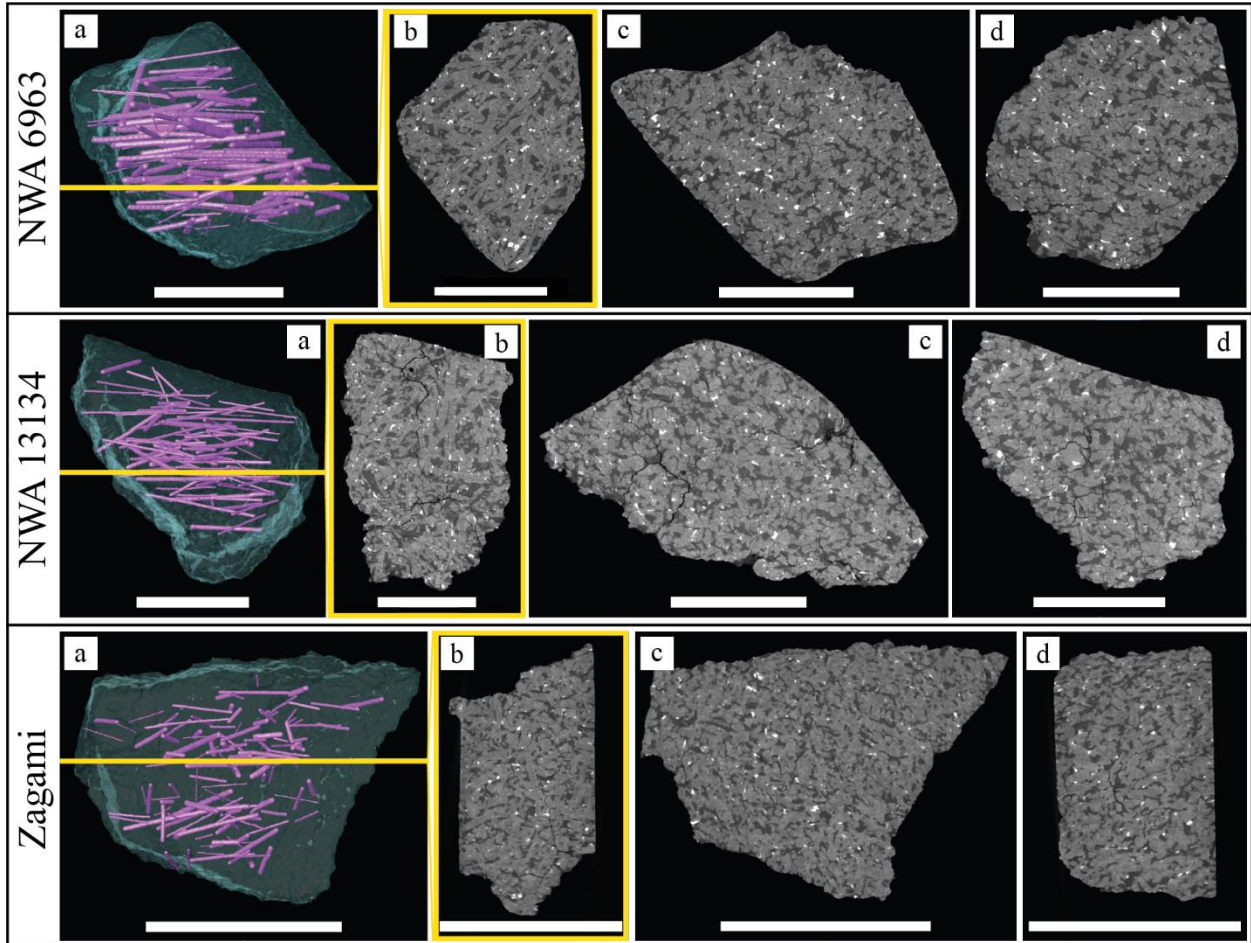
Figure 9



1094

1095
1096

Figure 10



1097
1098
1099

1100

1101

1102

1103

1104

1105

1106

1107

1108

1109

1110

1111

1112

1113

1114

1115

1116

FIGURE CAPTIONS

Figure 1: Grayscale CT slices for the olivine-phyric (a – d), basaltic (e – f), gabbroic (g), and poikilitic (h) shergottites in this study. The main phases are maskelynite, pyroxene, olivine (in olivine-phyric and poikilitic samples), and oxides/sulfides in order of increasing brightness. Scale bars are 1 mm.

Figure 2: 2D schematic showing the Quant3D workflow. (A) Grayscale CT data are segmented into their constituent phases (B). (C) Inset from (B) showing points randomly placed through phase-of-interest (i.e., white material) and cones emanating from each point along a set number of orientations. (D) The volume of each cone along every orientation is combined to create a tensor ellipsoid, from which eigenvectors and eigenvalues can be derived. The data can also be visually assessed with a 3D rose diagram. This process is shown here in 2D but is actually performed in 3D.

Figure 3: (A) 3D volume rendering of an elongated pyroxene crystal (transparent yellow) in NWA 13134 (10.8 mm x 0.8 mm x 0.5 mm) and a rod (light blue) drawn to represent the length and orientation of pyroxene crystal. A colored block illustrates 3 orthogonal orientations. (B) CT

1117 slice oriented orthogonally to the long axis of the same crystal highlighted in yellow (red
1118 orientation on block). (C and D) CT slices oriented along the long axes of the same crystal
1119 highlighted in yellow (blue and green orientations on block). Scale bars are 1 mm.

1120 **Figure 4:** Whole-rock and slice-by-slice modal abundances for the various phases within
1121 shergottites.

1122 **Figure 5:** Plot of CT fabric eigenvalue ratios after Woodcock and Naylor (1983) for different
1123 shergottite phases measured with Quant3D. Foliated fabrics are defined as $K < 1$, lineations
1124 defined as $K > 1$, triaxial defined as $K = 1$. Higher values of C correspond to stronger fabrics.
1125 Error bars represent 1σ standard deviation of 30 replicate analyses.

1126 **Figure 6:** Stereonets (lower hemisphere; equal area projection) showing the eigenvector
1127 orientations for each phase measured using Quant3D and the average orientation of high- μ
1128 phases measured with Blob3D (gray data). Each Quant3D data point represents one of the thirty
1129 replicate analyses. In general, a tight cluster of the third or first eigenvector, and a spread of the
1130 other two around a great circle, reflects a foliation or lineation, respectively. The high- μ Blob3D
1131 axes are not orthogonal because the average vector for each axis was calculated individually
1132 using a Bingham axial distribution (Fisher et al., 1993).

1133 **Figure 7:** Contoured stereonet (lower hemisphere; equal area projection) showing the
1134 orientation of individual pyroxene long axes. Each black dot represents a single crystal. The
1135 density of datapoints is reported in percent per 1% of stereonet area. Darker contours indicate a
1136 higher density of datapoints. Yellow lines represent foliation plane. See Figure 5 for meaning of
1137 K and C.

1138 **Figure 8:** Crystal size distribution (CSD) patterns for shergottite high- μ phases. The same bin
1139 sizes were used for all samples but the X- and Y-axes are scaled differently for each group. The
1140 gray columns represent data from bin sizes less than the turndown bin and are excluded from
1141 interpretations.

1142 **Figure 9:** CT slices with the minimum (left) and maximum (right) megacryst olivine or pyroxene
1143 oikocryst abundances for olivine-phyric and poikilitic shergottites, respectively. Scale bars are 2
1144 mm.

1145 **Figure 10:** (column A) 3D image showing whole-rock (transparent blue) with rods (magenta)
1146 that represent long axis of individual pyroxene crystals in NWA 6963, NWA 13134, and
1147 Zagami. (column B) CT slice oriented parallel to foliation plane (yellow line in [a]). (columns C
1148 and D) are CT slices oriented orthogonally to (B). All scale bars are 1 cm.